Warm conveyor belt characteristics and impacts along the life cycle of extratropical cyclones: Case studies and climatological analysis based on ERA5

Katharina Heitmann, Michael Sprenger, Hanin Binder, Heini Wernli, and Hanna Joos

Institute for Atmospheric and Climate Science, ETH Zurich, Zurich, Switzerland

Correspondence: Katharina Heitmann (katharina.heitmann@env.ethz.ch)

Abstract. This study presents a systematic and global investigation of the characteristics and impacts of warm conveyor belts (WCBs). For this purpose, we compile a new WCB climatology (1980–2022) of trajectories calculated with the most recent reanalysis dataset ERA5 from the European Centre for Medium-Range Weather Forecasts (ECMWF). Based on this new climatology, two-dimensional masks are defined, which represent the inflow, ascent and outflow locations of WCBs. These
5 masks are then used to objectively quantify the key characteristics (intensity, ascent rate, and ascent curvature) and impacts (precipitation and potential vorticity (PV) anomalies) of WCBs in order to (i) attribute them to different stages in the life cycle of the associated cyclones and to (ii) evaluate differences in the outflow of the cyclonic and anticyclonic branches.

The method is first tested and illustrated through three case studies of well-documented cyclones, revealing both the similarities and the case-to-case variability in the evolution of the WCB characteristics and impacts. We then extend the analysis to about
10 5'000 cyclones that occurred in winter between 1980–2022 in the North Atlantic. The case studies and the climatological analysis both show that WCBs are typically most intense (in terms of air mass transported, ascent rate, precipitation rate, and volume) during the intensification period of the associated cyclone. The northward displacement along the storm track and diabatic PV production lead to an increase in low-level PV in the region of WCB ascent during the cyclone life cycle. The negative PV anomaly at upper levels, associated with the WCB outflow, remains relatively constant. The investigation of the
15 WCB branches reveals an increasing intensity of the cyclonic WCB branch with time, linked to the increasing strength of the cyclonic wind field around the cyclone. Due to a lower altitude, the outflow of the cyclonic branch is associated with a weaker negative PV anomaly than the anticyclonic WCB branch, which ascends to higher altitudes. In summary, this study highlights the distinct evolution of WCB characteristics and impacts during the cyclone life cycle and the marked differences between the cyclonic and anticyclonic branches.

1 Introduction

The warm conveyor belt (WCB) is a coherent airstream that ascends from the warm sector of an extratropical cyclone into the upper troposphere, transporting moist air over large vertical and horizontal distances. It is one of the three main airstreams in an extratropical cyclone (Browning, 1990), which are the descending dry intrusion (Reed and Danielsen, 1958), the cold con-
25   veyor belt (Carlson, 1980), and the strongly ascending WCB (Harrold, 1973; Browning et al., 1973). The WCB was initially identified from the Eulerian flow field on isentropic surfaces (Namias, 1939; Carlson, 1980) and, more recently, by utilizing the Lagrangian perspective. Wernli and Davies (1997) defined the WCB as a "coherent ensemble of trajectories" by identifying trajectories in the vicinity of an extratropical cyclone (hereafter referred to as cyclone) that are associated with either a large decrease in pressure p, reduction in specific humidity q, or increase in potential temperature θ integrated along the trajectories.
30   Suitable thresholds to identify WCBs are about $600\,\mathrm{hPa}$ in two days for the ascent, $10\,\mathrm{g\,kg^{-1}}$ for the decrease in q, and $20\,\mathrm{K}$ for the increase in θ. WCBs occur in all seasons and in the mid-latitudes of both hemispheres but ascend most frequently in boreal winter in the North Atlantic (NA) and North Pacific (NP) storm tracks at around 30-50° N (Eckhardt et al., 2004; Madonna et al., 2014b). Eckhardt et al. (2004) also showed that most winter cyclones over oceans in the mid-latitudes are associated with a WCB. However, there is a broad spectrum of cyclones (Catto, 2016), which is also reflected in correspondingly large
35   case-to-case variability of the characteristics and impacts of WCBs.

In this study, we refer to "characteristics" as properties of WCBs that can be quantified from the number and paths of the trajectories, whereas with "impacts", we refer to effects of physical and dynamical processes in WCBs that affect meteorological variables like surface precipitation and potential vorticity (PV).

There are different measures to quantify such WCB characteristics and impacts. Regarding the characteristics of WCBs, previ-
40   ous studies investigated their intensity and ascent rate and the curvature of the ascending trajectories. The intensity of a WCB can be measured by the mass of air transported within the WCB, which can be quantified from a Lagrangian perspective as the number of WCB trajectories that form a coherent bundle and belong to the same cyclone. For instance, Binder et al. (2016) used this measure of WCB intensity and found a positive correlation with cyclone intensification. Another characteristic is the maximum ascent rate along the WCB trajectories (e.g., the maximum pressure decrease in $2\,\mathrm{h}$ along WCB trajectories, Rasp et al.,
45   2016; Oertel et al., 2019; Blanchard et al., 2020), which helps to distinguish between more gentle, slantwise ascent and faster updrafts due to embedded convection. This distinction corresponds to the "escalator-elevator concept" by Neiman et al. (1993). A third characteristic, the curvature of the WCB ascent, becomes apparent on horizontal maps of WCBs. WCBs, or branches of WCBs, can be categorized into anticyclonic (W1) and cyclonic (W2) WCB branches (Browning and Roberts, 1994; Wernli, 1997). The W1 branch typically enters an upper-level ridge downstream of the cyclone, joins the westerly upper-level jet, and
50   is characterized by an anticyclonic curvature during the ascent. The W2 branch, on the other hand, ascends near the cyclone center and therefore turns cyclonically during the ascent. In the case study of Wernli (1997), the W2 branch ascended further poleward and with lower initial specific humidity than the W1 branch. Martínez-Alvarado et al. (2014) found in a detailed case study that the anticyclonic W1 branch starts from lower latitudes and higher initial moisture contents, ascends to higher altitudes and thereby causes a stronger negative PV anomaly than the W2 branch. Blanchard et al. (2021) also found a higher

55 final altitude and lower PV values in the W2 branch compared to the W1 branch. The described WCB characteristics co-evolve with the life cycle of the associated cyclone as described in the detailed case study by Wernli (1997). For instance, the WCB was most intense before the cyclone reached its minimum central pressure, it ascended most rapidly in the early phase of the cyclone, and its curvature transitioned from anticyclonically to cyclonically as the cyclone intensified.

Important impacts of WCBs are related to surface precipitation and the diabatic production of PV anomalies in the lower and

60 upper troposphere, which both result from the ascent of moist air with subsequent cloud formation and latent heat release in the WCB. Traditionally, the WCB is regarded as the main precipitation-producing airstream in cyclones (Browning, 1990), and Pfahl et al. (2014) quantified that 70-80% of extreme precipitation events (6-hourly precipitation exceeding the 99th percentile) are linked to WCBs. This also holds specifically for the Mediterranean, where heavy precipitation in cyclones is predominantly associated with WCBs (Flaounas et al., 2018). Case study investigations of WCB ascent rates and surface precipitation (Binder,

65 2017; Oertel et al., 2019, 2020) revealed that intense local precipitation often occurs in regions of convection embedded in an ascending WCB. In contrast, more slowly slantwise ascending WCBs are typically linked to weaker precipitation rates. Another important impact of the WCB is the modification of PV at lower and upper levels, induced primarily by the wide range of cloud microphysical processes along the WCB ascent (Joos and Wernli, 2012; Joos and Forbes, 2016). To first order, PV is produced below the level of maximum latent heating and destroyed above, and vice versa for processes that consume latent

70 heat (e.g., Stoelinga, 1996; Wernli and Davies, 1997). This led to the general understanding that PV first increases along the ascent of the WCB in the lower troposphere until the level of maximum diabatic heating and then decreases again to similar values as at the start of the ascent (Wernli, 1997; Joos and Wernli, 2012; Madonna et al., 2014b; Methven, 2015). At the end of the ascent, in the so-called WCB outflow, the low PV values correspond to strongly negative PV anomalies because of the anomalously strong poleward and upward transport within the WCB and subsequent PV destruction (e.g., Grams et al., 2011;

75 Chagnon et al., 2013; Madonna et al., 2014b). The diabatic PV anomaly produced at low levels sometimes contributes to the rapid intensification of the associated cyclone (Binder et al., 2016). Accordingly, Booth et al. (2012) showed in a sensitivity experiment that enhanced latent heat release in the WCB due to higher surface temperatures leads to more intense cyclones. At higher levels, on the other hand, the diabatically produced negative PV anomalies potentially affect the flow evolution downstream of the cyclone. For instance, by supporting the negative PV anomaly of atmospheric blocks, WCBs likely enhance their

80 lifespan and intensity and support associated extreme weather events such as heat waves or cold air outbreaks (Pfahl et al., 2015; Steinfeld and Pfahl, 2019). When WCBs impinge on straight jets or less amplified Rossby wave patterns, they can either trigger the formation of Rossby waves (Röthlisberger et al., 2018) or contribute to wave amplification (Grams et al., 2011) or strengthening of the jet (Blanchard et al., 2021). Consistently, the diabatic processes in the WCB ascent were found to increase the forecast uncertainty in the region of the WCB outflow and further downstream (Grams et al., 2018; Rodwell et al., 2018).

85 This brief summary emphasizes the relevant impacts of WCBs on surface weather, the evolution of the associated cyclone, and the downstream flow. Because most of the studies so far focused on either one particular WCB impact or discussed the linkage between WCB characteristics and impacts in case studies, a systematic climatological analysis of WCB characteristics and impacts is currently missing. This study aims at closing this gap by using an established WCB identification method applied to state-of-the-art ERA5 reanalyses and then developing objective measures to obtain a climatology of WCB characteristics

90 and impacts. In combination with the tracking of cyclones, our approach will enable the systematic investigation of how WCB characteristics and impacts evolve along the life cycle of cyclones. Based on this approach, we aim to answer the following research questions first using case studies and later from a climatological perspective:

1. How do the characteristics and impacts of WCBs change along the life cycle of the associated cyclone?

95 2. How do specific characteristics and impacts of WCBs co-evolve along the life cycle of cyclones?

3. How do the cyclonic and anticyclonic WCB branches differ in terms of their characteristics and impacts?

Such an approach of systematically attributing specific properties to individual weather systems is very common for cyclones. Many studies described the properties of a cyclone in terms of a set of values that quantify, e.g., its lifetime, size, depth, intensity, intensification rate, and propagation speed (e.g., Neu et al., 2013). This study adds a next dimension to this feature-based

100 climatological approach by attributing an additional set of values, which quantify the characteristics and impacts of WCBs, to individual cyclone life cycles. In a subsequent study, we will use this methodology to attribute WCBs to cyclones in climate model simulations and investigate how the WCB characteristics and impacts might change in a future, warmer climate.

This study, focusing on cyclones and their WCBs in ERA5 data, first introduces the data and methods to quantify the characteristics and impacts of a WCB in Sect. 2. In Sect. 3, three case studies of cyclone life cycles and their WCB characteristics

105 and impacts are presented in detail, and in Sect. 4, the case study results are put into perspective by presenting a climatology of the temporal evolution of the characteristics and impacts of all WCBs in the North Atlantic in the winter seasons between 1980–2022. The main results are discussed and concluded in Sect. 5.

2 Data and methods

2.1 ERA5

110 For the scope of this study, we use the most recent reanalysis dataset ERA5 from the European Centre for Medium-Range Weather Forecasts (ECMWF) that represents the fifth generation of atmospheric reanalysis data (Hersbach et al., 2020). This dataset is characterized by 31 km spatial resolution (spectral resolution T369) on 137 model levels and hourly temporal resolution. We interpolate the output from ERA5 for the period 1980–2022 to a $0.5° \times 0.5°$ longitude-latitude grid to calculate trajectories, identify WCBs and calculate different metrics to describe them.

115

2.2 Cyclones and WCB trajectories

Cyclone masks are calculated according to the cyclone identification and tracking algorithm by Wernli and Schwierz (2006) that was further refined by Sprenger et al. (2017). The algorithm defines the cyclone mask by the outermost sea-level pressure (SLP) contour surrounding an SLP minimum, poleward of 25° N/S and with a maximum contour circumference of 7500 km.

120 Thereby, SLP minima associated with tropical convection or very large cyclone masks consisting of multiple cyclones are
avoided. Cyclone centers at consecutive times are combined into distinct cyclone tracks, which must last at least 24 h. Cyclone
tracks shorter than 24 h are neglected to omit transient and weak systems (see Sprenger et al., 2017 for details).

To identify WCBs, we use the Lagrangian analysis tool LAGRANTO (Wernli and Davies, 1997; Sprenger and Wernli, 2015).
Every six hours, 96 h forward trajectories are started. The trajectories are then calculated based on the three-dimensional wind

125 field with an hourly resolution. The starting positions are set globally on an 80 km equidistant grid in the lower troposphere
(790–1050 hPa every 20 hPa). To select WCB trajectories, we apply criteria adapted from the ones used by Madonna et al.
(2014b). First, WCB trajectories are defined as trajectories that ascend at least 600 hPa within 48 h. Then, a WCB bundle is
defined as a set of WCB trajectories that start within a 250 km distance to at least one other WCB trajectory, and a minimum of
one trajectory per WCB bundle must at least once coincide with a cyclone mask during its 48-hour ascent. Finally, a double-

130 count filter deletes trajectories that fulfill the previous WCB criteria at multiple time steps and would thus be counted several
times (see Madonna et al., 2014b for details). The WCB trajectory identification by Madonna et al. (2014b) was adapted in
two central aspects. First, the required threshold of 600 hPa for the decrease in pressure can be exceeded at any time during
the 48-hour ascent and not only strictly between the start and end of the ascent, 48 h later. Hence, we also take trajectories
into account that ascend rapidly and descend again within 48 h, which were not considered in the climatology by Madonna

135 et al. (2014b). Secondly, not all trajectories in a WCB bundle must be collocated with a cyclone mask at least once during the
ascent (as described above). The bundle of WCB trajectories also includes the eastern part of the WCB that potentially does
not coincide with the ETC mask at any point in time and therefore is excluded in the climatology by Madonna et al. (2014b).
The adapted WCB criteria are also described by Binder et al. (2020), who used them to investigate the vertical cloud structure
associated with a WCB. A climatology of the WCB trajectories in ERA5 based on this adapted definition can be found in Fig.

140 S1 in the supplementary material. In the comparison of the WCB climatology by Madonna et al. (2014b) with the present one
(Fig. S2), we found very similar starting regions of WCB trajectories and an eastward shift of the ascent and outflow location
in the new ERA5 climatology. Rapidly ascending trajectories, which are taken into account by the adapted WCB definition,
reach higher altitudes and higher zonal wind speeds at an earlier moment in their lifetime, thereby explaining the eastward shift
in the ascent and outflow locations. The ERA5 WCB climatology provides the basis for the calculation of the WCB masks,

145 which is described in the following section.

2.3 WCB masks

The WCB trajectories are used to define two-dimensional Eulerian WCB masks, representing different altitude ranges of the
WCB. More specifically, the 48-hour WCB can be divided into different altitude ranges depending on the pressure of the air

150 masses at a specific time. These altitude ranges are the WCB inflow (>800 hPa), ascent (500–800 hPa), and outflow (<400 hPa).
To avoid very large WCB outflow masks, we limit the maximum residence time in the WCB outflow region to 12 h after the
trajectories have crossed the lower limit of 400 hPa. These altitude ranges are used to analyze the impacts and characteristics
of WCBs at different phases during the ascent. For instance, we assume the ascent phase to be most important for forming

precipitation and modifying the low-level PV field. On the other hand, the outflow of the WCB likely coincides with negative
155 upper-level PV anomalies. Thus, by defining two-dimensional Eulerian masks for the different altitude ranges of WCBs, it is
possible to determine the impacts of WCBs separately for the different ascent phases of WCBs.

The WCB trajectories that define a WCB mask at time t^* can start between 0-48 h before t^*, as schematically shown in Fig.
2a. The positions of air parcels at t^* located in a specific pressure range (here WCB ascent, 500–800 hPa) are projected on a
latitude/longitude grid and then inflated to a circle with a 100 km radius (Fig. 2b). The envelope of these circles denotes the
160 outer border of all WCB air parcels in the respective ascent phase and therefore defines the two-dimensional Eulerian WCB
ascent mask at t^* (red line in Fig. 2b). By inflating the WCB air parcel position, artificial gaps in the masks in areas where
only a few WCB trajectories ascend are avoided. We only consider WCB trajectories for the mask calculation until the time
step when they have reached their minimum pressure in the 48-h ascent window. WCB masks are defined every six hours for
the entire ERA5 period for the inflow, ascent, and outflow pressure range. Additionally, we divide each WCB outflow mask
165 into sub-regions depending on the curvature of the trajectories inside the mask. For this purpose, we determine the curvature
of each WCB trajectory (see Sect. 2.4 for details of ascent curvature calculation) and separately calculate WCB outflow masks
for cyclonically, anticyclonically and noncurved WCB trajectories.

Previous studies also used two-dimensional masks to define the area of WCB ascent or outflow in order to study the relationship
between WCBs and PV streamers (Madonna et al., 2014a) or the co-occurrence of WCB masks, fronts, and intense precipitation
170 (Catto et al., 2015).

Based on the concept of defining WCBs in specific ascent phases as two-dimensional objects, we can now compile a new
WCB climatology that accounts for the variability of the ascent behavior of WCB trajectories. Figure 1 shows the frequency
of occurrence of WCB inflow (>800 hPa), ascent (500–800 hPa) and outflow (<400 hPa) masks. Key features of the new
climatology are consistent with previous WCB climatologies that are based on the location of WCB trajectories at different
175 time steps (Fig. S1; Stohl, 2001; Eckhardt et al., 2004; Madonna et al., 2014b), such as the enhanced frequency of WCB inflow
(Fig. 1a,b) in the region of the storm tracks and on the respective winter hemisphere. However, the inflation of each WCB
trajectory position to a 100 km circle leads to a distinct increase in the maximum frequency values from about 5–7% in Fig.
S1a to more than 25% in Fig. 1a. Another difference is the reduced frequency during the ascent phase compared to the inflow
and outflow phase. Typically, a bundle of WCB trajectories is less coherent (in terms of trajectories per area) in the inflow
180 and outflow region compared to the ascent region. Thus, WCB ascent masks tend to be smaller and spread over fewer grid
points, thereby causing a reduced frequency. One of the main advantages of a climatology based on WCB masks is the focus
on the different ascent phases of the WCB. Instead, taking the position of a WCB trajectory at a fixed time instance disregards
any information about the vertical position and is strongly dependent on the ascent behavior of a trajectory. For example, at
$t = 24$ h, WCB trajectories can be located at 700 hPa in the ascent phase or already at 300 hPa, thus, in the WCB outflow.
185 While these two WCB trajectory positions would be added to the same climatology ($t = 24$ h) in the previous method, the new
WCB climatology takes the different vertical positions into account and adds them to different climatologies (WCB ascent and
outflow).

Finally, each Eulerian WCB mask is linked to a cyclone by first attributing each bundle of WCB trajectories to the cyclone
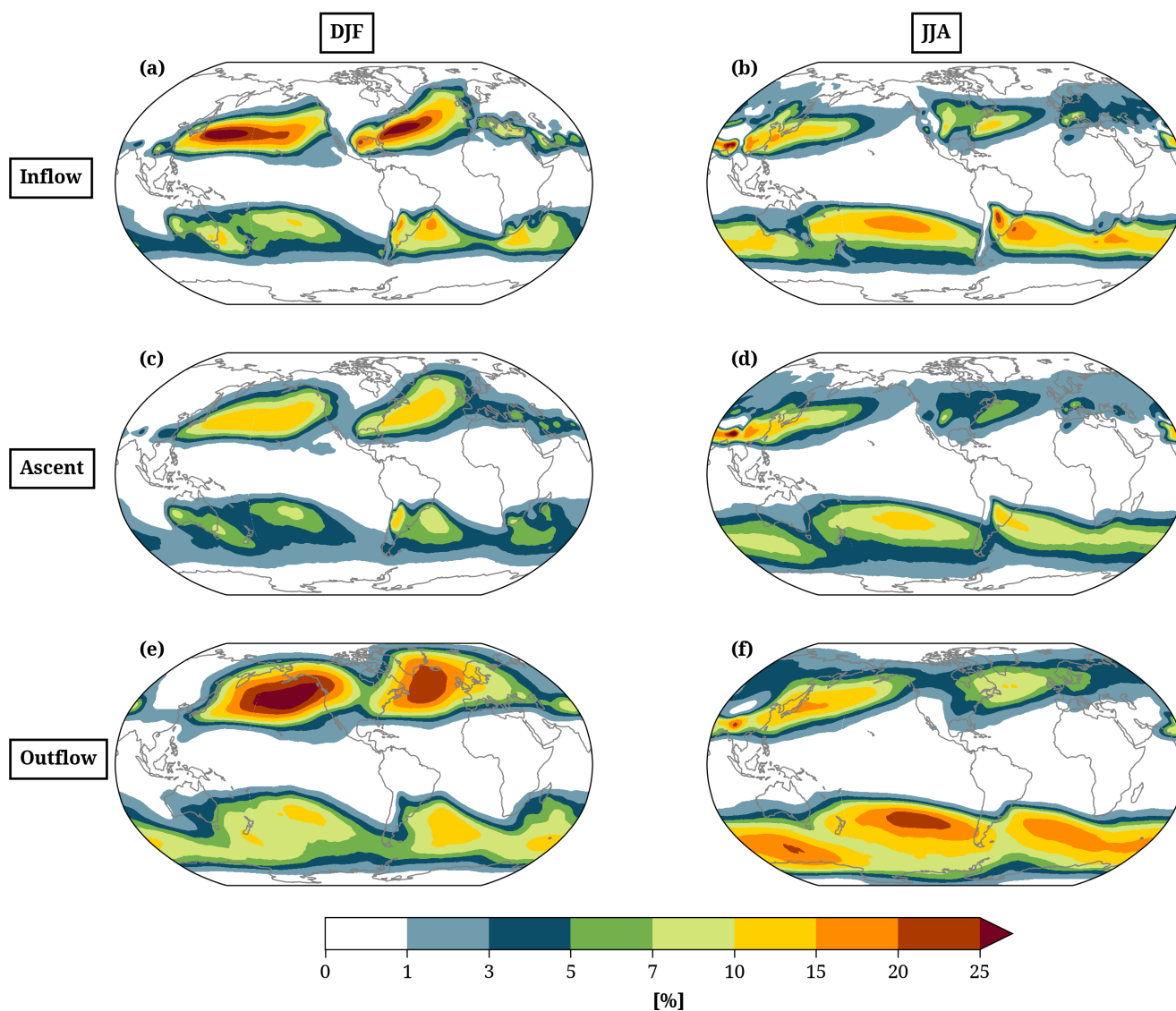
Figure 1. 42-year (1980–2022) climatology of the frequency of occurrence (%) of (a, b) WCB inflow, (c, d) ascent and (e, f) outflow masks in (left column) DJF and (right column) JJA. For each grid point, the number of time steps with a WCB mask present divided by the total number of time steps in the respective time period equals the frequency of occurrence.
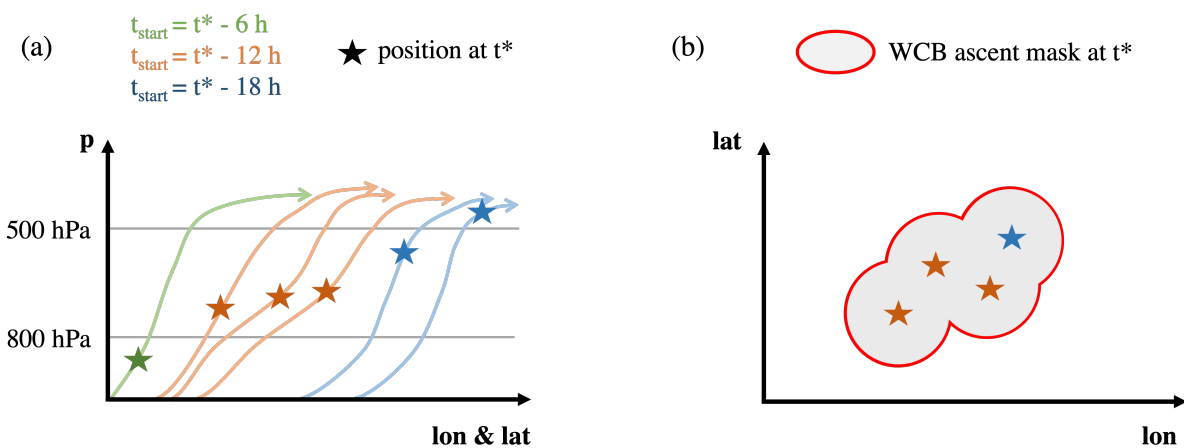
Figure 2. Schematic of WCB mask calculation. (a) 48-hour forward trajectories starting at different times and their location at time t^* (colored stars). (b) The horizontal position of trajectories that are located between 500–800 hPa at t^* (colored starts), 100 km radius around each position (grey circles) and final circumferent mask (red contour), defining the ascent region of a WCB. Schematic adapted from Catto et al. (2015).

with which they coincide most often. We only consider trajectory positions between 600–800 hPa when the WCB starts to

190 ascend distinctively and is located closest to the associated cyclone. In the second step, the cyclone linked to a WCB bundle is transferred to the resulting Eulerian WCB masks. Since different WCB bundles associated with different cyclones may define one WCB mask, we select the cyclone with which the largest number of trajectories is linked. The allocation of WCB masks to cyclones allows for analyzing the WCB characteristics and impacts during the cyclone life cycle.

195 **2.4 WCB characteristics and impacts**

To each WCB mask, we attribute metrics that describe the WCB's characteristics and impacts at a specific time instance. In general, WCB characteristics are calculated based on the properties of the WCB trajectories defining a WCB mask. In contrast, WCB impact metrics are derived from the statistical value of a variable (e.g., precipitation rate or low-level PV) over all grid points inside the two-dimensional Eulerian WCB mask. To clearly distinguish between a meteorological field (e.g.,

200 precipitation rate) and the resulting WCB impact metric, we use different abbreviations (e.g., PQ90) for the latter.

Three measures of **WCB characteristics** are calculated as follows:

－ **Intensity** The number of WCB trajectories inside a WCB ascent mask defines the WCB intensity. As trajectories start from an equidistant grid (Δx=80 km) and equally-spaced pressure levels (Δp=20 hPa), each trajectory represents a constant mass. Thus, the total number of trajectories in a WCB trajectory bundle represents the air mass that is transported

205   by the WCB. This concept was also applied by Binder et al. (2016), who quantified the WCB intensity accordingly and
        found a positive correlation with the cyclone deepening rate.

        – **Ascent rate** We define the WCB ascent rate as the mean pressure change of the trajectories that define the WCB ascent
        mask at a specific time step. For each trajectory, we calculate the pressure change during the last three hours prior to the
        arrival in the WCB ascent mask and then take the average over all trajectories. Short episodes of enhanced ascent rates
210   are also captured by taking a three-hour window.

        – **Ascent curvature** So far, the WCB curvature has never been investigated systematically. In a case study, Martínez-
        Alvarado et al. (2014) used the potential temperature at the end of the WCB ascent (48 h after the start of the trajectories)
        to identify the cyclonic and anticyclonic branches. However, this approach is unsuitable for a global and climatological
        study due to the decreasing tropopause height towards the poles, potentially creating a bias at high/low latitudes. Thus,
215   in the present study, we first classify each WCB trajectory based on its change in direction during the ascent and sub-
        sequently calculate the share of cyclonically or anticyclonically ascending trajectories in the WCB ascent mask. More
        specifically, the curvature of each individual trajectory is calculated as the mean change of direction (in degrees) between
        two time instances. The first time instance is defined as the time step the trajectory is first located at a pressure below
        600 hPa (t_{p600}). The second time instance is defined at the time step 12 h after t_{p600}, however, it must not exceed 48 h
220   after the starting time of the trajectory. The hourly change in direction between these two time instances is then aver-
        aged. By limiting the time span to a maximum of 12 h, we avoid the anticyclonic curvature that most WCB trajectories
        experience towards the end of the ascent and focus on the actual ascent direction. A mean change in direction of more
        than $4° \, h^{-1}$ is defined as a cyclonic ascent, and a change in the direction of less than $-2° \, h^{-1}$ is defined as an anticy-
        clonic ascent. Ascent curvature values in between are defined as a straight or weakly curved ascent. The thresholds were
225   chosen based on multiple case studies. To quantify the ascent curvature of the WCB mask, we define it as the ratio of
        cyclonically or anticyclonically curved trajectories to the total number of trajectories that define a WCB mask. Figure
        3 illustrates the WCB case described by Martínez-Alvarado et al. (2014) and how the different WCB branches are well
        identified with the presented method except for a few trajectories that are classified as cyclonically ascending (green)
        although turning eastward, likely due to an initial strong cyclonic curvature. However, we found in several case studies
230   that this objective method results in a reasonable identification of WCB branches. In this case and at this moment in
        time, cyclonic/anticyclonic/non-curved trajectories account for 25%/7%/68% of the WCB.

        – **Altitude** To characterize where the WCB outflow masks are located vertically, we calculate the median pressure of all
        trajectories located in a WCB outflow mask at each time instance. This metric will be used to study differences in the
        outflow of the different WCB branches.

235   The four **WCB impacts**, related to precipitation and PV, are quantified as follows:

        – **Precipitation rate and volume (PQ90, PVOL)** We quantify the precipitation rate associated with each WCB at a spe-
        cific time by calculating the 90th percentile of total precipitation rates (convective + large-scale precipitation rate, PQ90)
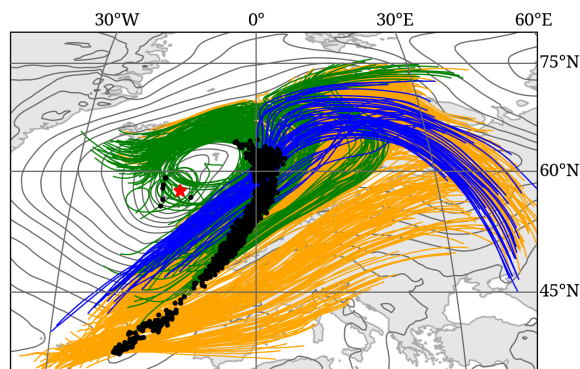
Figure 3. 48-h WCB trajectories for the dichotomous WCB case described by Martinez-Alvarado et al. (2014), located between 500–800 hPa at 00 UTC on 25 November 2009 (black dots) and ascending cyclonically (green), anticyclonically (blue), or without a distinct curvature (orange). The red star marks the position of the cyclone center, and grey contours show SLP (every 4 hPa) at 00 UTC on 25 November 2009.

of all grid points inside the WCB ascent mask. This metric thereby also captures small-scale areas of locally intense precipitation. Additionally, for each grid cell inside the WCB ascent mask, we calculate the volume of precipitation (grid

240 cell area times precipitation rate). The sum of these precipitation volumes over all grid cells inside a WCB ascent mask equals the total precipitation volume (PVOL) of the WCB at a specific time over one hour.

– **Low-level PV (LLPV)** The precipitation formation along the WCB leads to the release of latent heat. The vertical gradient in the diabatic heating rates leads to PV production below the heating maximum. To quantify the impact of WCBs on the PV distribution at low levels, we first calculate vertically averaged PV between 750–950 hPa at each grid

245 point inside the WCB ascent mask. Since the background PV at lower altitudes is relatively small (approx. 0.5 pvu) and exhibits only a weak seasonal cycle, we take the in situ values instead of the anomaly. We calculate the low-level PV metric (LLPV) of a WCB mask as the 90th percentile of the vertically averaged PV values of the grid points inside the mask. The 90th percentile was chosen because the area of enhanced PV values often accounts only for a small part of the whole WCB ascent mask.

250 – **Upper-level PV anomaly (ULPVA)** Diabatic PV destruction above the level of maximum latent heat release and upward advection of low-PV air masses in a WCB leads to a region of anomalously low PV values in the area of WCB outflows. To quantify this impact, we first vertically average PV at all grid points inside a WCB outflow mask between 200–375 hPa. The monthly 42-year climatology of vertically averaged PV over the same pressure range is then subtracted to get a PV anomaly. The subsequent upper-level PV anomaly (ULPVA) is defined as the median of the anomaly values of

255 all grid points inside the WCB outflow mask. As the negative upper-level PV anomaly often accounts for a majority of the region of WCB outflow, the median is a reasonable measure to quantify it.

In addition to the WCB's characteristics and impacts, we also quantify the evolution of the cyclone that is linked to each WCB mask (see last paragraph in Sect. 2.3) using the central pressure and its deepening rate. Sanders and Gyakum (1980) defined the deepening rate ΔSLP_B as the change in minimum SLP over 24 h, normalized by $\frac{sin(60°)}{sin(\phi)}$, where ϕ refers to the mean latitude of

260 the cyclone center during this time interval. The calculation implies a minimum cyclone lifetime of 24 h. Rapidly intensifying cyclones with a maximum $\Delta \text{SLP}_B > 1$ Bergeron are referred to as "bombs" (Sanders and Gyakum, 1980). The evolution of the deepening rate along the life cycle of each cyclone allows for defining the time step of the most intense deepening as the center of the 24-h period that results in the largest ΔSLP_B. The WCB masks are attributed not only with metrics describing their characteristics and impacts but also their position in time relative to the time step of the most intense deepening of the

265 associated cyclone.

To summarize, the resulting data set consists of 42 years (1980–2022) of two-dimensional Eulerian WCB mask objects that define the WCB inflow, ascent, and outflow region every six hours and globally. A set of metrics describes the characteristics and impacts of each WCB mask. Attributing each WCB mask to a specific cyclone allows for an investigation of the WCB metrics along the cyclone life cycle. Additionally, we calculated individual outflow masks and their characteristics and impacts,

270 defined by the cyclonic and anticyclonic WCB branches.

3 Case studies

We first utilize the developed method to assess the characteristics and impacts of WCBs in three case studies of North Atlantic cyclones. Starting with case studies serves two purposes: it enables a relatively detailed analysis of how WCB characteristics and impacts relate to the overall synoptic-scale setting and evolution of the cyclones, and it helps to identify the strengths and

275 limitations of the method. Readers more interested in the climatological analysis of WCB characteristics and impacts may jump directly to Sect. 4. After performing about 10 detailed case studies, three cyclones were selected to be presented here, which (i) are well-documented in the literature and therefore known to the community, and (ii) reveal interesting similarities and differences. The first case was an extremely strong cyclone that occurred in January 1989 and that was associated with intense precipitation. The second case in November 2009 featured a clear separation of the cyclonic and anticyclonic WCB

280 branches. The third case in November 1992 revisits the first WCB that was investigated in detail based on trajectory calculations (Wernli, 1997). Due to the complex synoptic situations associated with the 2009 and 1992 cases, we manually attributed WCB trajectories to the respective cyclone. The limitations of an objective attribution of WCBs and cyclones are discussed in Sect. 5. For all cases, we start with a qualitative discussion of WCB characteristics and impacts at selected time steps before discussing quantitatively the evolution of the WCB metrics along the life cycle of the cyclones.

285 ### 3.1 Case 1: January 1989, ERICA IOP4, North Atlantic

The Experiment on Rapidly Intensifying Cyclones over the Atlantic (ERICA) took place at the beginning of 1989. During the fourth period of intense observations (IOP4), a cyclone formed off the US east coast and later developed into the most extreme cyclone in this region until then, with a minimum SLP of 936 hPa, and a deepening rate of 3.4 Bergeron (Neiman and Shapiro,
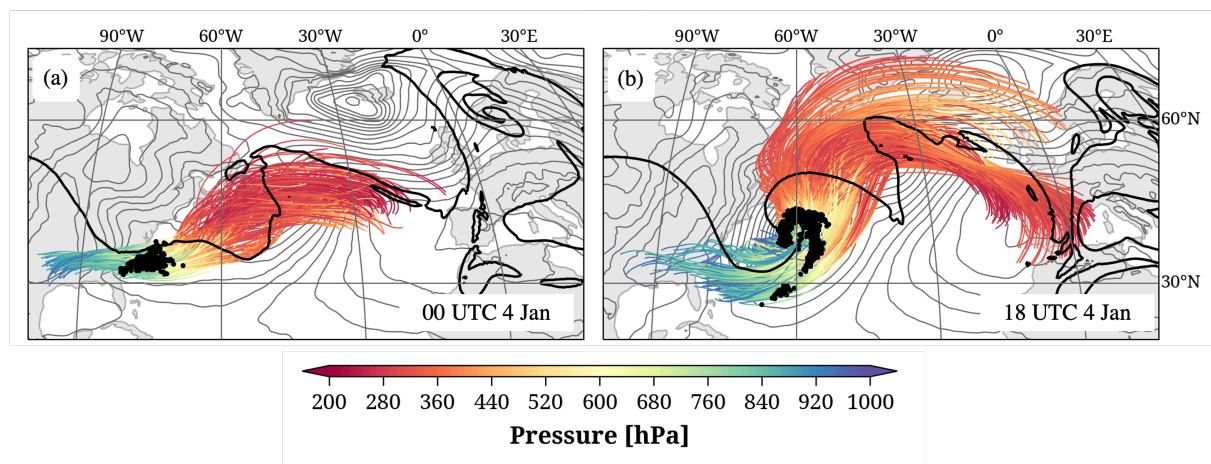
Figure 4. 48-hour WCB trajectories (colored by pressure; hPa) associated with Case 1 (ERICA IOP4 cyclone). Trajectories are shown that contribute to the WCB ascent mask (500–800 hPa) at (a) 00 UTC and (b) 18 UTC on 4 January 1989. Black dots mark the position of the WCB air parcels at the respective time step, grey contours show SLP (every 4 hPa), and the black dashed line is the 2-pvu contour at 320 K at the respective time.

1993). The development of the frontal structures of this cyclone was analyzed and discussed in detail in Neiman and Shapiro
290 (1993) and Neiman et al. (1993). The latter study described the associated WCB as a southerly airstream that ascended over the
warm front during the early phase of cyclogenesis. Doppler-radar cross sections of the vertical velocity and reflectivity at the
warm front at 06 UTC on 4 January 1989 showed that the WCB consisted of a combination of rapidly and slowly ascending
sub-airstreams, which Neiman et al. (1993) referred to as "elevator vs. escalator" ascent. While the life cycle of the ERICA
IOP4 cyclone is well documented, the temporal evolution of the associated WCB has not been investigated. In the following,
295 we describe the characteristics and impacts of this WCB at individual time steps and investigate their evolution along the
cyclone life cycle.

3.1.1 WCB characteristics

Figure 4 shows all WCB trajectories associated with the ERICA IOP4 cyclone that contributed to the WCB ascent mask at two
specific time steps. At 00 UTC on 4 January 1989 (Fig. 4a), the weak cyclone is located off the US east coast and ahead of a
300 relatively broad upper-level trough (indicated by the 2-pvu contour on 320 K). The 209 trajectories that define the associated
WCB ascent mask originate over the southeastern US and ascend gradually from west to east (Fig. 4a). During their main ascent
phase, the WCB turns northeastward and mainly remains a coherent bundle of trajectories. The position of the trajectories at
this moment in time (indicated by black dots in Fig. 4a) coincides with the location of the developing cyclone. Later, in the
WCB outflow, the trajectories turn eastward along the upper-level flow.
305 During the next 18 h, the cyclone intensifies strongly while moving eastward, and the upper-level trough wraps up cyclonically
(cyclonic wave breaking, Thorncroft et al., 1993). At 18 UTC on 4 January (Fig. 4b), 579 trajectories contribute to the WCB
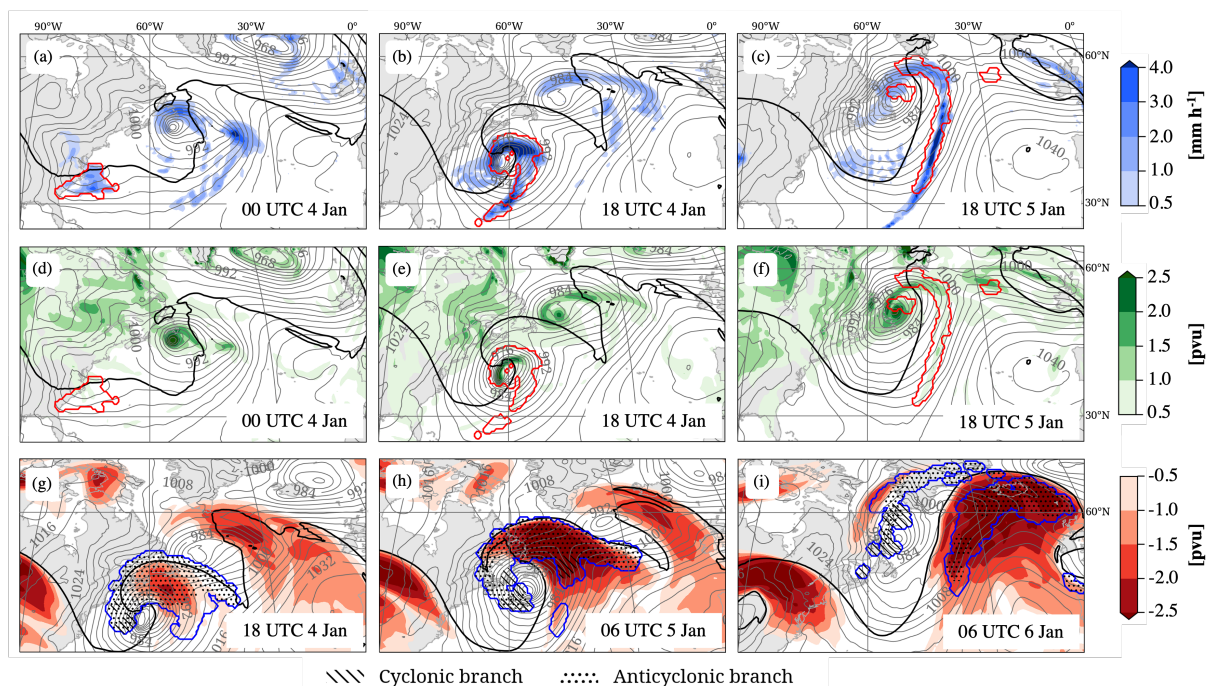
Figure 5. WCB-related impacts of Case 1 in terms of (a-c) precipitation rate (mm h^{-1}, blue shading), (d-f) low-level PV (pvu, green shading), and (g-i) upper-level PV (pvu, red shading) as well as the location of the WCB ascent and outflow masks (red and blue contours, respectively), SLP (grey contours every 4 hPa) and 2-pvu contour on 320 K (pvu, black line). The hatching in the WCB outflow mask indicates the outflow of the cyclonic (dashed) and anticyclonic (dotted) WCB branches (see text for details). All fields are shown at the times indicated in the lower right of the panels. Note that times differ when showing the WCB ascent (a-f) and WCB outflow (g-i).

ascent mask, i.e., the WCB more than doubled its intensity. Some of these trajectories still originate from the southeastern US, but most have their starting positions in the western North Atlantic. In contrast to the situation 18 h before, the WCB trajectories turn poleward during their ascent and strongly diverge at upper levels. Most WCB trajectories ascend rapidly near
310 the cyclone center, while some trajectories ascend along the cold front. The WCB ascent mask (given by the envelope of the black dots in Fig. 4b) nicely agrees with the T-bone frontal structure described by Neiman et al. (1993), with a short warm, and prominent bent-back front. At this time, the WCB outflow reaches much more poleward than 18 h before, contributing to the formation of a prominent ridge downstream of the cyclone. Similar to the situation at 00 UTC on 4 January, the trajectories turn anticyclonically at upper levels, and some trajectories descend slightly towards Europe. Thus, by examining the WCB at
315 two individual time steps 18 h apart, we can already observe a qualitative shift in the characteristics of the WCB.

3.1.2 WCB impacts

We now investigate the precipitation rate and low-level PV in the region of the WCB ascent as well as the upper-level PV anomaly in the region of the WCB outflow at selected time steps along the cyclone life cycle. Early in the life cycle, at 00 UTC

on 4 January (Fig. 5a), the cyclone is associated with weak precipitation mainly near the center and south of it in the warm

320   sector. The precipitation signal aligns almost perfectly with the WCB ascent mask (red contour in Fig. 5a and black dots in Fig. 4a). During the following 18 h, when the cyclone and WCB both strongly intensify, precipitation also becomes considerably more intense. At 18 UTC on 4 January (Fig. 5b), the most intense precipitation occurs northeast of the cyclone center and along the cold front ($> 4\,\mathrm{mm\,h^{-1}}$). Again, the vast majority of precipitation occurs inside the WCB ascent mask. Weak precipitation rates behind the cold front are not associated with the WCB ascent (most likely shallow cumulus convection in the cold sector).

325   A day later, at 18 UTC on 5 January (Fig. 5c), the cyclone center has moved poleward and has been overtaken by the upper-level trough, and the WCB ascends mainly along the elongated cold front. Precipitation is strongest along the cold front inside the WCB ascent mask, and precipitation near the cyclone center has strongly decreased.

At 00 UTC on 4 January (Fig. 5d), the region of the cyclone is characterized by low PV values at low levels (750–950 hPa), which are most likely not yet strongly enhanced by latent heating. After the strong cyclone intensification in the following

330   18 h, a region of enhanced low-level PV ($> 2.5\,\mathrm{pvu}$) is located along the bent-back front, within the WCB ascent (Fig. 5e). We note that the intense signal of PV at low levels along the bent-back front (Fig. 5e) agrees well with the observation-based analyses in Neiman et al. (1993) who showed very intense low-level PV in this region associated with a westerly low-level jet exceeding $35\,\mathrm{m\,s^{-1}}$ (their Fig. 18). In contrast, the region of the WCB ascent along the cold front does not show enhanced low-level PV values. After the cyclone intensification, PV values remain high near the cyclone center, where a small fraction

335   of the WCB ascends (Fig. 5f). In addition, the elongated region of the WCB ascent along the cold front is also associated with enhanced low-level PV values. At this moment, regions of enhanced precipitation rates (Fig. 5c) and low-level PV coincide to some extent, which is consistent with diabatic PV production.

The upper-level PV anomalies and the WCB outflow masks are illustrated in Fig. 5g-i. At 18 UTC on 4 January (Fig. 5g), i.e., after the cyclone has strongly intensified, WCB trajectories arrive in the upper troposphere, spread out, and fill the entire

340   amplifying upper-level ridge. The majority of the WCB outflow is formed by anticyclonically curved trajectories (see Sect. 2.3 for details concerning the mask calculation for the different branches). Only a small region in the southwest corresponds to the outflow of the cyclonic WCB branch. In the center of the WCB outflow mask, northeast of the cyclone center, a moderate negative PV anomaly has developed with values around $-1.5\,\mathrm{pvu}$. The ULPVA in the outflow of the anticyclonic branch equals $-0.5\,\mathrm{pvu}$, while it is strongly positive ($3.4\,\mathrm{pvu}$) in the small outflow region of the cyclonic WCB branch, which coincides with

345   the upper-level trough. Twelve hours later (Fig. 5h), due to the northward progression of the ridge and the intensified WCB outflow, the negative PV anomaly has intensified in terms of its area and amplitude. A large part of the upper-level ridge is characterized by an upper-level PV anomaly with values below $-2.5\,\mathrm{pvu}$, which aligns almost exactly with the outflow region of the anticyclonic WCB branch (ULPVA$= -2.1\,\mathrm{pvu}$). Similar to the previous time instance, the WCB outflow west of the cyclone center is formed mainly by the cyclonic branch and is associated with a positive ULPVA of $1.7\,\mathrm{pvu}$, potentially because

350   of the low altitude and latitude of the WCB outflow in this region. A day later, at 06 UTC on 6 January (Fig. 5i), most of the WCB outflow mask is located in the upper-level ridge that developed downstream of the cyclone and is mainly formed by the anticyclonic WCB branch. Inside the outflow mask of the anticyclonic branch, the ULPVA equals $-2.2\,\mathrm{pvu}$, while the minimum of the entire PV anomaly has values below $-2.5\,\mathrm{pvu}$. Similar to the previous time step, in the westernmost part of
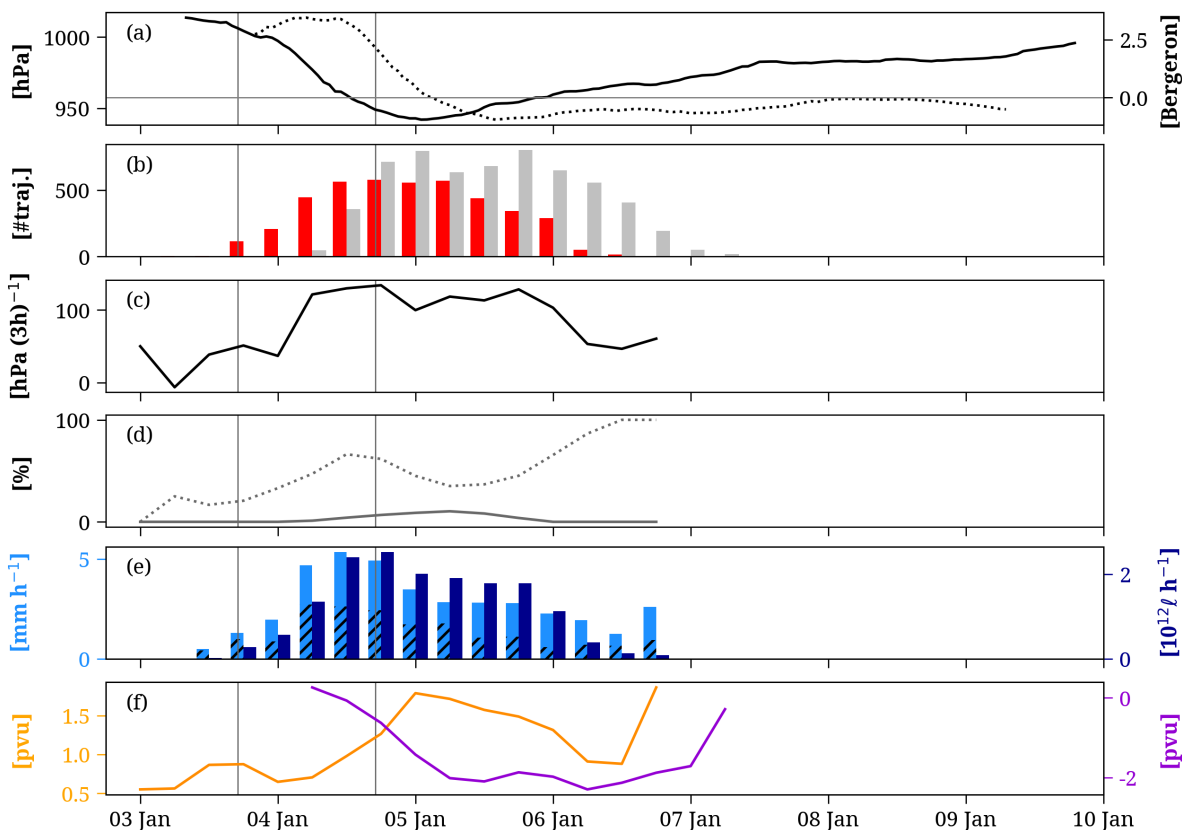
Figure 6. Temporal evolution of cyclone characteristics and WCB characteristics and impacts for Case 1: (a) the cyclone's central pressure (solid, hPa) and deepening rate in the center of 24-h window (Bergeron, dotted), (b) intensity of WCB ascent (number of trajectories, red) and outflow (number of trajectories, grey), (c) mean ascent rate (hPa $(3\,\text{h})^{-1}$), (d) percentage of cyclonically (%, solid) and anticyclonically ascending trajectories (%, dotted), (e) convective precipitation (mm h^{-1}, hatched) and PQ90 (mm h^{-1}, light blue) and PVOL ($10^{12}\,\ell\,\text{h}^{-1}$, dark blue), and (f) LLPV (pvu, orange) and ULPVA (pvu, violet). Vertical lines denote the 24 h period of strongest cyclone intensification.

the WCB outflow below the upper-level trough, no or only a weak negative PV anomaly is discernible. This part of the WCB outflow is largely formed by the cyclonic WCB branch with a ULPVA of 0.6 pvu in its outflow region. To conclude, similar to the WCB characteristics, also the impacts of the WCB evolve during the cyclone life cycle.

3.1.3 Evolution of WCB metrics

We now quantify the characteristics and impacts of the WCB according to Sect. 2.4 and investigate their temporal evolution along the entire cyclone life cycle. Figure 6a shows the central pressure and deepening rate of the cyclone, which was first detected at 09 UTC on 3 January 1989. After an initial weak intensification, the deepening rate reaches about 3.4 Bergeron in the 24-h window around 05 UTC on 4 January, consistent with Neiman and Shapiro (1993). The cyclone reaches its minimum

SLP of $942\,\mathrm{hPa}$ at 01 UTC on 5 January and gradually weakens over the following five days (partially shown). The WCB associated with this very intense cyclone also evolved with time. As already indicated in Fig. 4, the intensity of the WCB varied with time (Fig. 6b). First, the number of trajectories in the WCB ascent mask increases for about a day before reaching a

365   maximum of 572 trajectories at the end of the most substantial cyclone intensification period. It then gradually decreases once the cyclone has reached its minimum pressure. The intensity of the WCB outflow evolves similarly but is delayed by about $12\,\mathrm{h}$ and shows a second local maximum during cyclone decay. At 18 UTC on 5 January, a maximum of 804 trajectories define the WCB outflow mask. In terms of ascent rate, the largest values ($136\,\mathrm{hPa}\,(3\,\mathrm{h})^{-1}$) occur at the time of maximum intensity of the WCB ascent (Fig. 6c). The ascent rates were distinctively lower ($< 52\,\mathrm{hPa}\,(3\,\mathrm{h})^{-1}$) at the early stages of the WCB

370   evolution. As previously seen in Fig. 4a, the WCB first ascends without a distinct ascent curvature, but with time, the share of anticyclonically ascending trajectories increases until it reaches 100% at 18 UTC on 6 January (Fig. 6d). The cyclonic branch, however, remains weak over the entire cyclone life cycle, and it maximizes with 10.3% about $6\,\mathrm{h}$ after the time of maximum cyclone intensity.

The impacts of the WCB also vary with time, as shown in Fig. 6e,f. The precipitation rate, PQ90, increases rapidly during

375   the cyclone's intensification phase and reaches a maximum of $5.3\,\mathrm{mm}\,\mathrm{h}^{-1}$ at 12 UTC on 4 January (Fig. 6e, light blue). This peak value occurs along the bent-back front $6\,\mathrm{h}$ before the field shown in Fig. 5b. Afterward, the precipitation intensity slowly weakens (see also Fig. 5c). The relative share of convective precipitation decreases steadily with time along the cyclone life cycle, indicating that embedded convection is most prominent in the early phase of the cyclone when it is located at low latitudes. The precipitation volume, PVOL, reaches a maximum value of $2.5 \cdot 10^{12}\,\ell\,\mathrm{h}^{-1}$ towards the end of the main cyclone

380   intensification phase at 18 UTC on 4 January (Fig. 6e, dark blue). Considering PV, the cyclone's intensification is associated with an increase in LLPV to maximum values above $1.5\,\mathrm{pvu}$ (Fig. 6f, orange line). This PV is diabatically produced and related to the strong precipitation formation near the cyclone center within the WCB ascent mask (Fig. 5e). LLPV values decrease once the cyclone reaches its minimum pressure. The brief increase in LLPV at 18 UTC on 6 January is not robust, as only a few WCB trajectories ascend at this time. At upper levels, the ULPVA intensifies rapidly in the $24\,\mathrm{h}$ after 06 UTC on 4

385   January, simultaneously with the intensity of the WCB outflow. This intensification of ULPVA was also apparent in Fig. 5g,h. The most intense ULPVA ($-2.3\,\mathrm{pvu}$) occurs at 06 UTC on 6 January, $36\,\mathrm{h}$ after the time of maximum cyclone intensity (Fig. 5i). Thereafter, the ULPVA weakens.

As will become clearer when discussing the climatological results in Sect. 4, the WCB of the IOP4 cyclone was very intense in terms of the number of WCB trajectories, the ascent rate, precipitation rate, and volume, as well as LLPV before the cyclone

390   reached its deepest SLP. At upper levels, the WCB outflow intensity increased simultaneously with the intensity of the ULPVA, both peaking 24–36 h after the cyclone reached its minimum SLP.

3.2   Case 2: November 2009, North Atlantic

In November 2009, UK scientists performed a research flight into a North Atlantic cyclone with a prominent WCB to test their experimental setup for the North Atlantic waveguide and downstream impact experiment in 2016 (NAWDEX, Schäfler et al.,

395   2018). Knippertz et al. (2010) analyzed a vertical profile along the flight and found an enhanced moisture content between
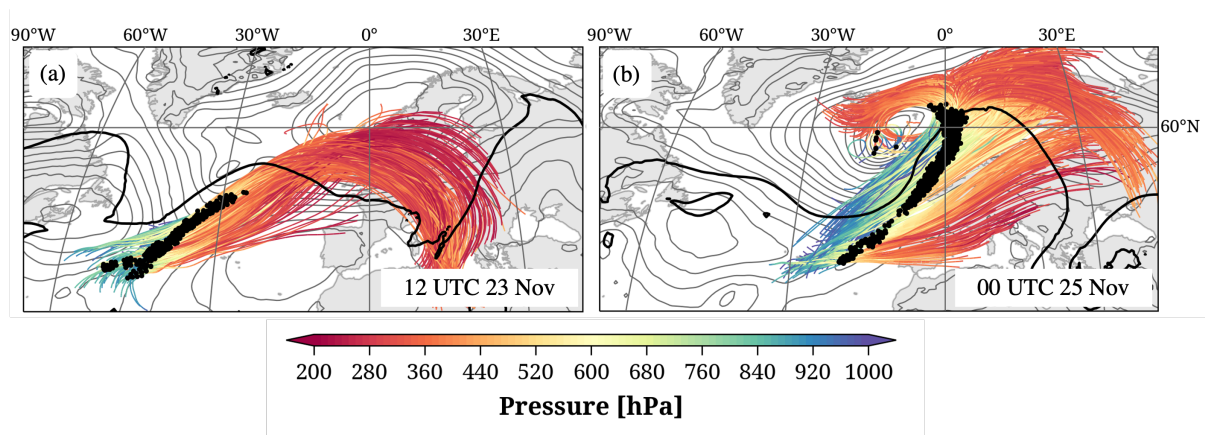
Figure 7. As Fig. 4 but for Case 2 trajectories that are located in the WCB ascent pressure range at (a) 12 UTC on 23 November and (b) 00 UTC on 25 November 2009.

770–900 hPa, linked to the ascent of the WCB from the moist planetary boundary layer. Numerical simulations of this WCB were investigated in detail by Martínez-Alvarado et al. (2014) as it featured a distinct split at its northern end into an anticyclonic (W1) and a cyclonic (W2) branch. The W1 branch initially had higher values of q, ascended along the cold front south of the cyclone, and arrived at higher outflow altitudes than the cyclonically curved W2 branch. The split of the WCB into these two branches was reported to occur early in the WCB's evolution. We selected this well-documented WCB case to assess how well our method identifies the different WCB branches and their respective characteristics. In addition to the analysis of the WCB branches, we investigate the characteristics and impacts of the WCB at individual time steps as well as along the cyclone life cycle.

3.2.1 WCB characteristics

The cyclone and its associated WCB are shown at two different time steps in Fig. 7. Thirteen hours after genesis, at 12 UTC on 23 November 2009 (Fig. 7a), the developing cyclone is located at about 30°W and 50°N, southwest of a mature cyclone. At upper levels, a high-PV trough is located upstream of the cyclone, indicated by the 2-pvu line on 320 K. The WCB trajectories that define the ascent mask at this moment start at the southern tip of the PV trough and ascend in an elongated region ahead of it (indicated by black dots in Fig. 7a). The bundle of trajectories remains coherent during the ascent and without a distinct curvature. At upper levels, the trajectories flow into the developing ridge downstream of the cyclone and thereby turn anticyclonically. The WCB becomes less coherent over the following 36 h and can be divided into three branches at 00 UTC on 25 November(Fig. 7b), about a day after the time of strongest intensity of the associated cyclone. WCB trajectories ascending along the northern part of the cold front turn anticyclonically (W1), while trajectories ascending close to the cyclone center turn cyclonically (W2). WCB trajectories starting from the southern end of the cold front ascend without a distinct curvature
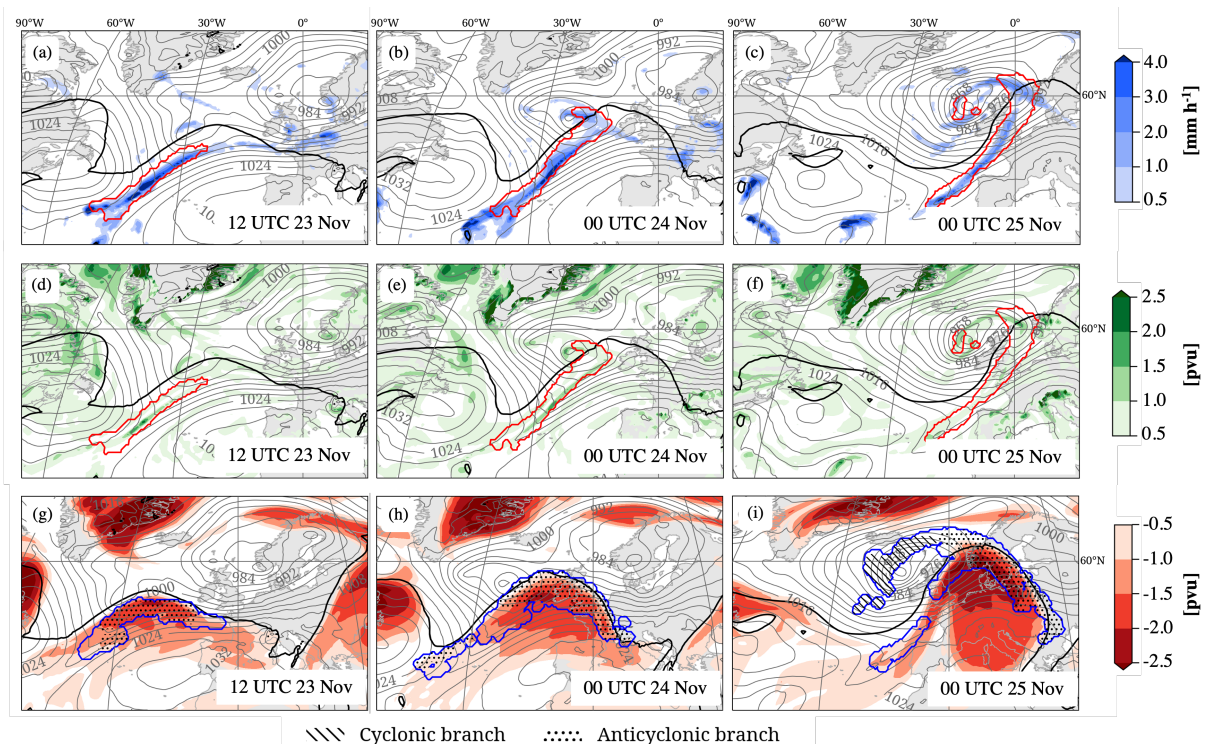
Figure 8. As Fig. 5 but for Case 2 (22–29 November 2009) at the times indicated in the lower right of each panel.

(non-curved) and are located at 315 hPa 48 h later, 30 hPa above the rest of the WCB trajectory bundle. The classification of the trajectories into three branches depending on their change in direction during the ascent was also illustrated in Fig. 3 (see Sect. 2.4). In contrast, Martínez-Alvarado et al. (2014) distinguished two WCB branches based on the potential temperature at the end of the ascent of WCB trajectories that were calculated with different limited-area models (COSMO, Met Office Unified

420   Model) and started at 18 UTC on 23 November. However, the pathway of these trajectories is very similar to the trajectories shown in Fig. 7b. Intriguingly, the branch classification based on the change in direction results in very similar conclusions regarding the characteristics of the WCB branches as in Martínez-Alvarado et al. (2014). Compared to W2, W1 has higher initial values of q (about 9 vs. 8 g kg^{-1}) and experiences stronger latent heating such that its outflow occurs on a higher isentrope (about 310 vs. 305 K). However, the PV increase during the WCB ascent is larger for W2 (peak values of 0.9 vs. 0.7 pvu),

425   consistent with the study by Martínez-Alvarado et al. (2014) that found the strongest PV increase along WCB branches that start further north and ascend close to the cyclone center.

3.2.2 WCB impacts

Figure 8 shows the precipitation rate, low-level PV, and upper-level PV anomaly in the region of the WCB ascent and outflow

430 at three selected time steps. The WCB ascent mask at 12 UTC on 23 November (defined by the trajectories shown in Fig. 7a) and the precipitation rate are shown in Fig. 8a. The band of WCB ascent aligns well with an elongated band of precipitation, with the most intense precipitation located in its center ($> 4\,\mathrm{mm\,h^{-1}}$). No significant precipitation occurs at this moment in the emerging cyclone center. Twelve hours later (Fig. 8b), the region of WCB ascent has moved eastward, and the cyclone has intensified. The WCB ascends along the elongated cold front as well as close to the cyclone center. The most intense

435 precipitation still occurs along the cold front, but weak precipitation also forms near the cyclone center. Weak precipitation along the cyclone's warm front, south of Ireland, is not associated with the WCB ascent. A day later (Fig. 8c), the cyclone has intensified noticeably while moving northeastwards. The WCB ascent mask (defined by trajectories shown in Fig. 7b) reaches from around 40°N to 65°N and coincides with the cyclone's cold front. The northwestward extension of the WCB ascent mask at high latitudes indicates the split of the WCB as illustrated in Fig. 7b. The majority of precipitation is still formed along the

440 cyclone's cold front, inside the WCB ascent mask, and with enhanced intensity at lower latitudes. The warm front and cyclone center are associated with only weak precipitation rates.

Prior to cyclone intensification, the WCB ascent mask coincides with an elongated band of enhanced low-level PV (Fig. 7d). A small region of distinctively enhanced values embedded in this band aligns with the previously described region of intense precipitation rates (Fig. 7a). The cyclone center is characterized by only weakly enhanced low-level PV values at this moment.

445 Twelve hours later (Fig. 7e), the low-level PV distribution in the region of WCB ascent is still similar. The region of most enhanced low-level PV coincides with the region of most intense precipitation rates at this time (Fig. 7b). A region of enhanced low-level PV close to the cyclone center is slightly outside of the WCB ascent mask. Note that in an idealized study, Schemm and Wernli (2014) explained this by diabatic low-level PV production beneath the WCB and subsequent westward advection at low levels into the cyclone center. At 00 UTC on 25 November (Fig. 7f), almost the entire region of WCB ascent is associated

450 with low-level PV values between 0.5–2 pvu. The precipitation rates in the region of most intense low-level PV values are no longer distinctively enhanced. Near the cyclone center, low-level PV values are enhanced and partially coincide with WCB ascent.

At upper levels at 12 UTC on 23 November (Fig. 8g), some WCB trajectories arrive at the northern edge of the ridge that develops downstream of the cyclone. The emerging ridge is characterized by a negative upper-level PV anomaly with the most

455 intense values (approx. -2 pvu) in the region of the WCB outflow, which is mainly formed by anticyclonically curved WCB trajectories. The ULPVA in the outflow region of the anticyclonic branch equals -1.6 pvu. The area of the negative PV anomaly increases during the following 12 h when the ridge becomes more pronounced (Fig. 8h). Similar to the previous time step, the most intense PV anomaly is located in the northern part of the ridge and in the region of WCB outflow. The ULPVA inside the outflow region of the anticyclonic branch, which makes up the majority of the entire WCB outflow mask, has become less

460 intense and equals -1.2 pvu. At 00 UTC on 25 November (Fig. 8i), the split in the WCB trajectory bundle becomes apparent. The WCB outflow along the northeastern edge of the ridge is formed by the anticyclonic WCB branch and coincides with
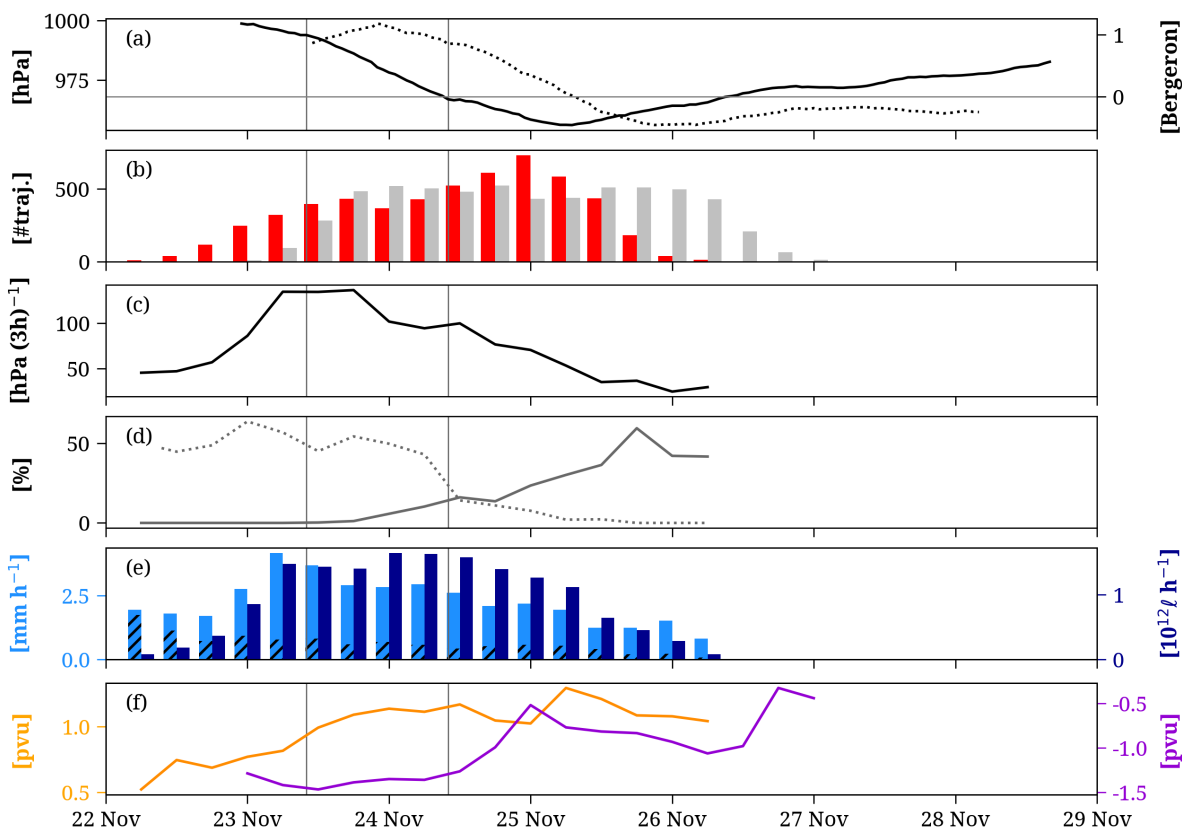
Figure 9. As Fig. 6 but for the cyclone and WCB in Case 2 (22–29 November 2009).

the negative PV anomaly inside the ridge, while the outflow of the cyclonic branch bends towards the cyclone center. As a result, the ULPVA inside the outflow of the anticyclonic branch equals -1.2 pvu, whereas the outflow of the cyclonic branch is characterized by a ULPVA of 1.4 pvu.

465

3.2.3 Evolution of WCB metrics

Figure 9 shows the evolution of the WCB's characteristics and impacts along the cyclone life cycle. The cyclone forms at 23 UTC on 22 November and starts its main intensification phase at 10 UTC on 23 November (Fig. 9a). The cyclone classifies as a bomb cyclone with a maximum deepening rate of 1.2 Bergeron at 22 UTC on 23 November. The pressure in the cyclone's

470 center continues to decrease after the main intensification phase and finally reaches a minimum of 956.2 hPa at 07 UTC on 25 November. Afterward, the cyclone weakens for four days before it disappears. The intensity of the WCB increases in two phases (Fig. 9b). The first WCB ascent mask appears at 06 UTC on 22 November. After that, the number of WCB trajectories in the ascent phase increases to 456 at 18 UTC on 23 November, followed by a slight weakening. Finally, 733 WCB trajectories

ascend at 00 UTC on 25 November, shortly before the cyclone reaches its minimum SLP. Thereafter, the number of trajectories
in the WCB ascent decreases rapidly. The WCB first reaches the region of WCB outflow at 00 UTC on 23 November, 18 h
after the first appearance of the WCB ascent mask. After a rapid increase in WCB outflow intensity, it remains constant for
about 2.5 days and, after that, decreases rapidly.

The WCB trajectories that ascend in these two phases differ in their characteristics. The first peak in WCB intensity is associated
with rapidly ascending trajectories (up to $134 \, \text{hPa} \, (3 \, \text{h})^{-1}$, Fig. 9c), which ascend mainly anticyclonically (Fig. 9d). During the
second peak in WCB intensity, the WCB trajectories ascend slower, many of them cyclonically.

The impacts of the WCB also vary over time. The first phase of enhanced WCB intensity is associated with the most intense
PQ90 (Fig. 9e, light blue), potentially linked to the enhanced ascent rates of the WCB during this phase (Fig. 9c). The convective
precipitation rate decreases as the cyclone and WCB ascent regions move poleward. During the cyclone's main intensification
period, PQ90 remains at around $2.6 \, \text{mm} \, \text{h}^{-1}$, before it decreases gradually. The resulting PVOL (Fig. 9e, dark blue) peaks
18 h after the peak in PQ90. The increasing WCB intensity and area of the ascent mask are most likely responsible for this
shift compared to PQ90. However, PVOL also peaks a day before the WCB reaches its maximum intensity. The decreasing
PQ90 could explain why PVOL and WCB intensity do not peak simultaneously. Once the WCB intensity decreases, PVOL
also decreases rapidly.

As shown above, the precipitation formation along the cold front and cyclone center leads to diabatic PV modification. LLPV
increases from $0.5 \, \text{pvu}$ to more than $1 \, \text{pvu}$ along the cyclone life cycle (Fig. 9f, orange line). The northward movement and,
thus, an increase in the Coriolis parameter can explain why LLPV remains high at later stages in the cyclone life cycle, although
latent heating becomes weaker. The evolution of the Coriolis parameter along WCB trajectories and the resulting importance
for the production of high low-level PV was investigated in detail by Madonna et al. (2014b). The authors linked the gradual
increase of the Coriolis parameter along WCB trajectories that started from a region in the North Atlantic to their poleward
ascent direction (see their Fig. 11d).

Finally, we consider the evolution of ULPVA. It was most intense during cyclone intensification ($-1.5 \, \text{pvu}$, purple line) when
the WCB outflow covered mainly the northern edge of the ridge that developed downstream of the cyclone. The increase in
the intensity of the cyclonic branch leads to a decreasing ULPVA. As shown in Fig. 8i, the outflow of the cyclonic branch is
located west of the ridge and in a region of weak PV anomalies in the considered layer. Thus, ULPVA equals $-0.5 \, \text{pvu}$ at 00
UTC on 25 November. Afterward, ULPVA slightly intensifies again when the cyclonic WCB branch transports low-PV air
from the ridge towards the northwest (not shown in Fig. 8). The weakening ULPVA in the final phase of the WCB outflow is
less robust due to the small number of WCB trajectories at this moment.

This case study was characterized by a distinctive split of the WCB into prominent branches with cyclonic and anticyclonic
curvature during the ascent. Our method identified these branches and the differences in their characteristics well, as the
comparison with Martínez-Alvarado et al. (2014) showed. Furthermore, we found that the increase in the share of cyclonically
ascending trajectories during the cyclone life cycle is associated with a decrease in WCB ascent rate, PQ90, a weakening of
ULPVA, but an increase of LLPV.
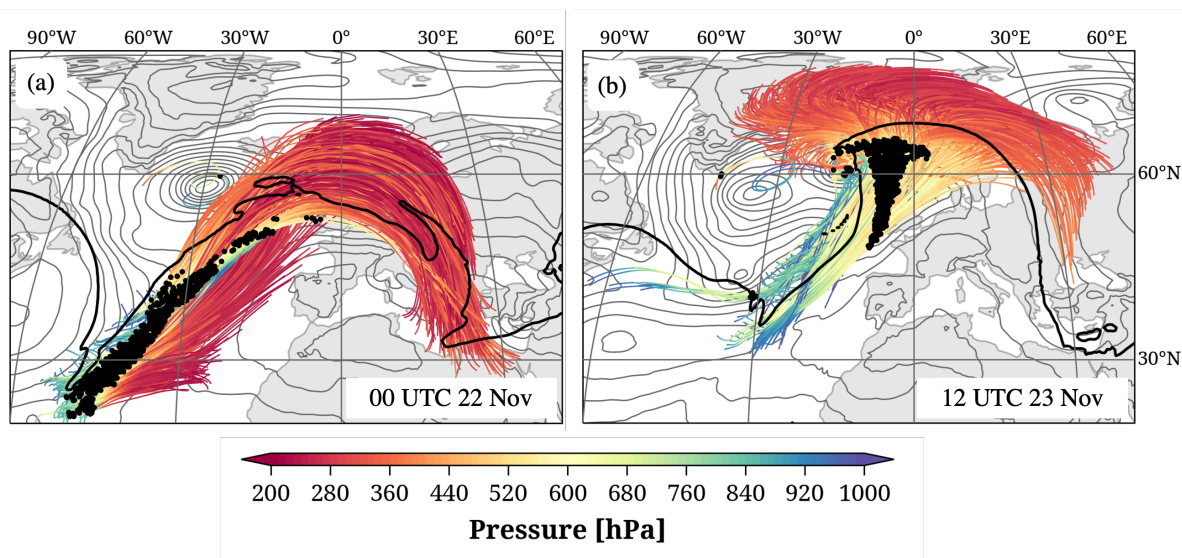
Figure 10. As Fig. 4 but for Case 3 trajectories that are located in the WCB ascent pressure range at (a) 00 UTC on 22 November and (b) 12 UTC on 23 November 1992.

3.3 Case 3: November 1992, North Atlantic

The application of the Lagrangian perspective to define and investigate WCBs from analysis data was first introduced by
Wernli and Davies (1997), who applied Lagrangian selection criteria to a large set of trajectories and thereby identified WCBs
as coherent bundles of trajectories in cyclones. Selecting trajectories that either experienced a strong pressure decrease, strong
moisture decrease, or a strong increase in potential temperature resulted in very similar WCBs. In Wernli (1997), the authors
investigated in detail a cyclone that formed in the North Atlantic in November 1992, which was associated with two WCBs,
one ascending in the vicinity of the cyclone center and the other one along the trailing cold front. At upper levels, both
airstreams split into anticyclonic and cyclonic branches, with the share of cyclonically ascending trajectories increasing with
time. The number of trajectories that fulfilled the ascent criterion varied with time, with the largest number of WCB trajectories
identified between 12 UTC on 22 November and 12 UTC on 24 November, i.e., during the main period of cyclone deepening.
The same cyclone was investigated by Rossa et al. (2000), who focused on the formation of a prominent PV-tower associated
with this cyclone. They showed that latent heating in ascending trajectories and associated diabatic PV production was mainly
responsible for the middle and lower parts of the PV-tower. The ascending trajectories associated with the PV-tower's middle
part resembled one of the WCBs identified by Wernli (1997). In the following, we will revisit this cyclone and apply our
methods to quantify the characteristics and impacts of this well-studied WCB and investigate how they evolved along the
cyclone life cycle.

3.3.1 WCB characteristics

525 The cyclone formed in a complex synoptic situation, which complicates the association of WCB trajectories to the cyclone in the early phase of its life cycle. As described by Wernli (1997) and illustrated in Fig. 10a, the cyclone develops at 00 UTC on 22 November 1992 from a frontal wave that is located south of the mature cyclone at 30°W and 60°N. At upper levels, an elongated high-PV trough extends from about 25°N to 60°N. The trajectories that fulfill the WCB criteria come from two different source regions that are not clearly separated. The majority of trajectories ascend at low latitudes ahead of the trough,

530 while a secondary airstream ascends in close proximity to the developing cyclone, in agreement with Wernli (1997). We combined both airstreams into one WCB, which ascends at this moment without a distinct curvature. At upper levels, the WCB trajectories flow into the ridge that develops downstream of the cyclone. In the following 1.5 days, the cyclone intensifies rapidly and moves poleward while the ridge downstream of the cyclone intensifies (Fig. 10b). The WCB trajectories start at low latitudes but mainly ascend further northward and east of the cyclone in a T-shaped region, consistent with the cyclone's

535 intense bent-back front (Rossa et al., 2000). WCB trajectories ascending at lower latitudes ascend mainly without a distinct curvature, while trajectories ascending at higher latitudes first ascend cyclonically but then turn anticyclonically at higher altitudes. A small fraction of the WCB ascends strictly cyclonically toward the cyclone center. Figure 10b also shows impressively the large area extending from Greenland to eastern Europe covered by the WCB outflow.

3.3.2 WCB impacts
540

Figure 11 shows the WCB-related impacts in the region of WCB ascent (Fig. 11a-f) and WCB outflow (Fig. 11g-i). At 00 UTC on 22 November (Fig. 11a), the elongated PV trough southwest of the mature cyclone leads to the formation of an elongated band of precipitation along its eastern flank. The precipitation formation coincides almost entirely with the WCB ascent mask. Precipitation rates are especially intense at low latitudes ($> 4\,\mathrm{mm\,h^{-1}}$). 18 h later (Fig. 11b), the WCB ascends not only along

545 the cold front but also near the center of the emerging cyclone located at 20°W and 55°N. Similar to the previous time step, the majority of the cyclone's precipitation coincides with the WCB ascent mask, and the most intense precipitation rates occur along the cold front, consistent with Wernli (1997). Weak precipitation along the cyclone's warm front is not related to the WCB ascent. Another 18 h later (Fig. 11c), the cyclone has noticeably intensified, and the WCB ascent mask, defined by the trajectories shown in Fig. 10b, coincides with weak precipitation rates along the weakening cold front and with more intense

550 precipitation rates along the warm and bent-back fronts.

The cyclone forms at 00 UTC on 22 November in proximity to a small region of enhanced low-level PV (1.5–2 pvu, Fig. 11d), located at 20°W and 47°N. The region of WCB ascent, mainly located southwest of the local PV maximum, aligns with a band of mildly enhanced low-level PV. In contrast, 18 h later (Fig. 10e), the region of intense precipitation along the cyclone's cold front is also associated with a band of distinctively enhanced low-level PV (1.5–2 pvu). The diabatically produced PV

555 linked to the precipitation formation along the ascending WCB is consistent with findings by Rossa et al. (2000). In addition, low-level PV is also enhanced near the cyclone center, coinciding with intense precipitation rates. After the strong cyclone
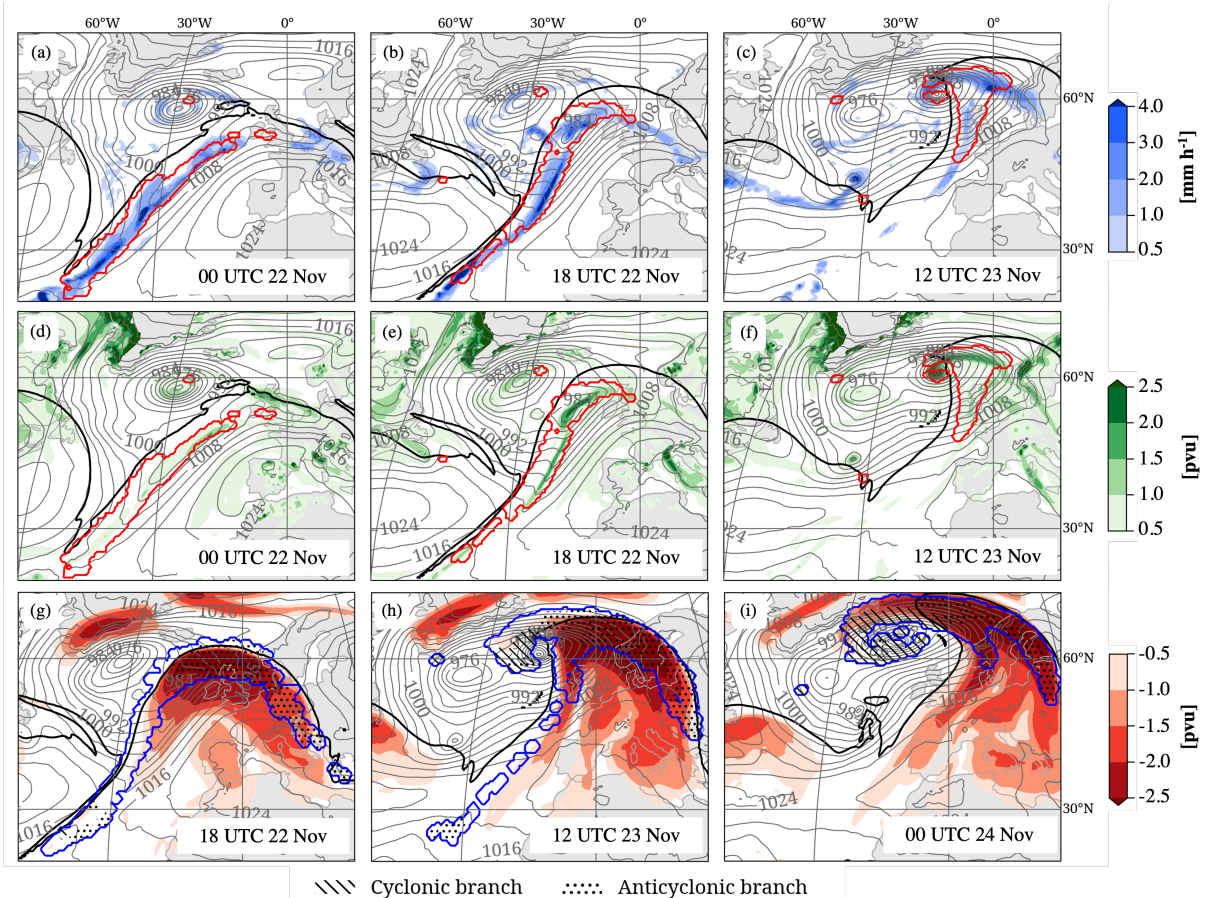
Figure 11. As Fig. 5 but for Case 3 (19–25 November 1992) at the times indicated in the lower right of each panel. Note that times differ when showing the WCB ascent (a-f) and WCB outflow (g-i).

intensification (Fig. 10f), low-level PV is mainly enhanced along the warm front and near the cyclone center but less intense along the cold front. The strongly enhanced PV values in the cyclone center formed the lower part of the PV-tower described by Rossa et al. (2000). The WCB ascent mask coincides with the described regions of enhanced PV inside the cyclone. At this

560   moment, precipitation rates and low-level PV values correlate less than at the previous time step. As we only take PV values between 750–950 hPa into account, enhanced PV values above this pressure range will not be detected.

The WCB arrives at upper levels first at 18 UTC on 22 November (Fig. 10g) in an elongated band that extends from the southern end of the PV trough to the northern end of the ridge that develops downstream of the cyclone. The intense negative PV anomaly (< -2.5 pvu) associated with the ridge coincides with the WCB outflow of the anticyclonic branch, which is char-

565   acterized by a ULPVA of -2.3 pvu. In the following 1.5 days (Fig. 10h), the negative PV anomaly intensifies while the ridge moves poleward and eastward. Similar to the previous time instance, the PV anomaly coincides strongly with the outflow of the anticyclonic branch (ULPVA$= -2.1$ pvu). The outflow of the cyclonic branch extends to a region of weak/no upper-level
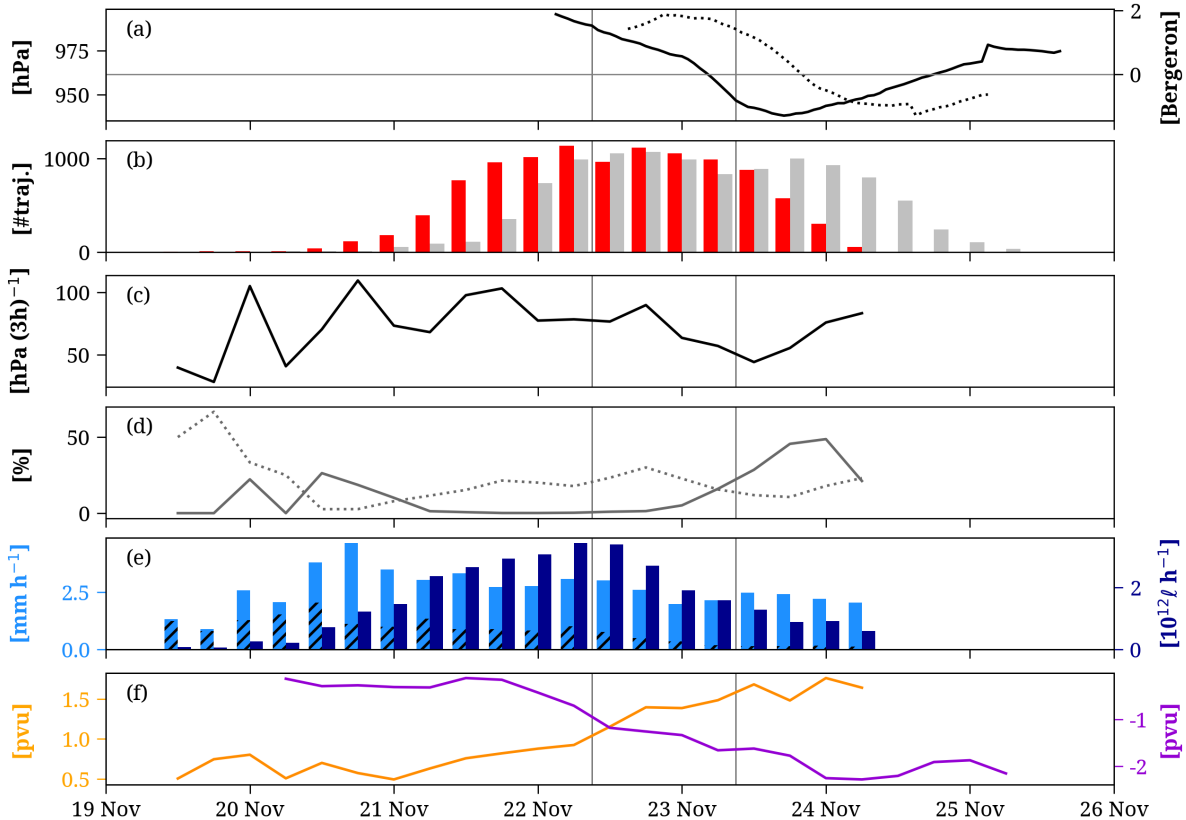
Figure 12. As Fig. 6 but for the cyclone and WCB in Case 3 (19–25 November 1992).

PV anomalies in the west of the ridge and towards the cyclone center. As a result, the ULPVA inside the outflow mask of the cyclonic branch equals $0.4\,\mathrm{pvu}$. The interpretation of the slightly positive value is that here the WCB outflow is at a lower altitude compared to the anticyclonic branch, and therefore the tropopause is close to its climatological position (leading to a weak anomaly in the layer considered for the calculation of ULPVA). At 00 UTC on 24 November (Fig. 10i), the ridge extends towards the west due to the cyclonic WCB branch that advects anomalously low-PV air from the ridge towards the west. Thus, the ULPVA inside the outflow of the cyclonic branch becomes slightly negative ($-0.4\,\mathrm{pvu}$). In contrast, the outflow of the anticyclonic branch is still associated with a strongly negative ULPVA of $-2.7\,\mathrm{pvu}$.

3.3.3 Evolution of WCB metrics

The temporal evolution of the cyclone, as well as the characteristic and impact metrics that describe the WCB, are shown in Fig. 12. The cyclone is first discernible at 03 UTC on 22 November 1992 with a central pressure of $995.4\,\mathrm{hPa}$ (Fig. 12a). After an initial weak intensification phase of about a day, the central pressure decreases rapidly at 00 UTC on 23 November. The cyclone

580   reaches its minimum pressure (938.3 hPa) at 17 UTC on 23 November and afterward weakens slowly. The rapid decrease in pressure results in a maximum deepening rate of 1.9 Bergeron at 19 UTC on 22 November. As previously described, the ascent of the WCB is first mainly driven by upper-level forcing and later influenced by the cyclone. The WCB ascent mask is first identified at 12 UTC on 19 November (red bars, Fig. 12b), 2.5 days before the genesis of the cyclone. The temporal delay is linked by the manual attribution of the trajectories to the later emerging cyclone. In the initial phase of the WCB evolution,

585   only a small number of trajectories ascend at low latitudes south of the developing PV trough (not shown). Only when the WCB starts to ascend ahead of the PV trough at around 00 UTC on 21 November the WCB intensity increases distinctively. The WCB reaches its maximum intensity at 06 UTC on 22 November with 1136 trajectories and remains very intense for the following day, coinciding with the cyclone's main intensification period. After the cyclone's most rapid intensification period, the WCB weakens and vanishes after about a day. A small number of WCB trajectories arrive in the WCB outflow region at

590   06 UTC on 20 November (grey bars, Fig. 12b). With a delay of approx. one day relative to the WCB ascent, also the WCB outflow intensity increases. About 1000 trajectories remain in the WCB outflow region until 00 UTC on 24 November, when the number of trajectories decreases gradually.

The movement of the WCB ascent region from low to high latitudes could explain the decrease in the WCB ascent rate with time (Fig. 12c). While the incipient WCB ascends with more than $100\,\mathrm{hPa}\,(3\,\mathrm{h})^{-1}$, the ascent rate decreases to $44\,\mathrm{hPa}\,(3\,\mathrm{h})^{-1}$

595   after the cyclone's main intensification period. The curvature of the WCB also evolves with time, as qualitatively described above. The WCB starts as a mainly straight flow; large variations at early stages are caused by a small number of trajectories and are thus statistically less robust (Fig. 12d). While the number of trajectories increases drastically, the relative intensity of the W1 and W2 branches remains relatively constant. Towards the end of the cyclone's intensification period, the share of W2 starts to increase, while W1 remains at a relatively constant percentage. This finding is consistent with Wernli (1997),

600   who already described the split of the WCB and an increase in the intensity of the cyclonic branch with time. The decreased intensity of the W2 branch at 06 UTC on 24 November is linked to the relatively small total number of trajectories and, thus, less robust statistics.

Figure 11 already showed that the WCB ascent mask coincides well with the cyclone-related precipitation. PQ90 is most intense ($4.6\,\mathrm{mm}\,\mathrm{h}^{-1}$, light blue bars in Fig. 12e) at 18 UTC on 20 November, in the early stages of the WCB's evolution, when

605   it ascended mainly at low latitudes. The northward movement is associated with a decrease in PQ90 and a decline in the share of convectively formed precipitation. However, PVOL (dark blue bars in Fig. 12e) peaks later at the beginning of the cyclone's intensification period. This delay is due to the increased WCB ascent mask area with WCB intensity. Before the WCB intensity increases distinctively, LLPV remains between 0.5–1 pvu for the first 1.5 days (orange line, Fig. 12f). Once the WCB starts to intensify noticeably, LLPV increases until it reaches 1.7 pvu briefly after the main cyclone intensification period. The diabatic

610   PV production and the increase of the Coriolis parameter towards the north both contribute to the increase in LLPV. At upper levels, ULPVA (purple line, Fig. 12f) remains weak until 12 UTC on 21 November, when the first significant amount of air transported by the WCB reaches higher altitudes. The ULPVA then intensifies to about -2.3 pvu at 00 UTC on 24 November and persists until the WCB outflow mask disappears.

In summary, the importance of the WCB in this case study for the precipitation formation and diabatic PV formation, as
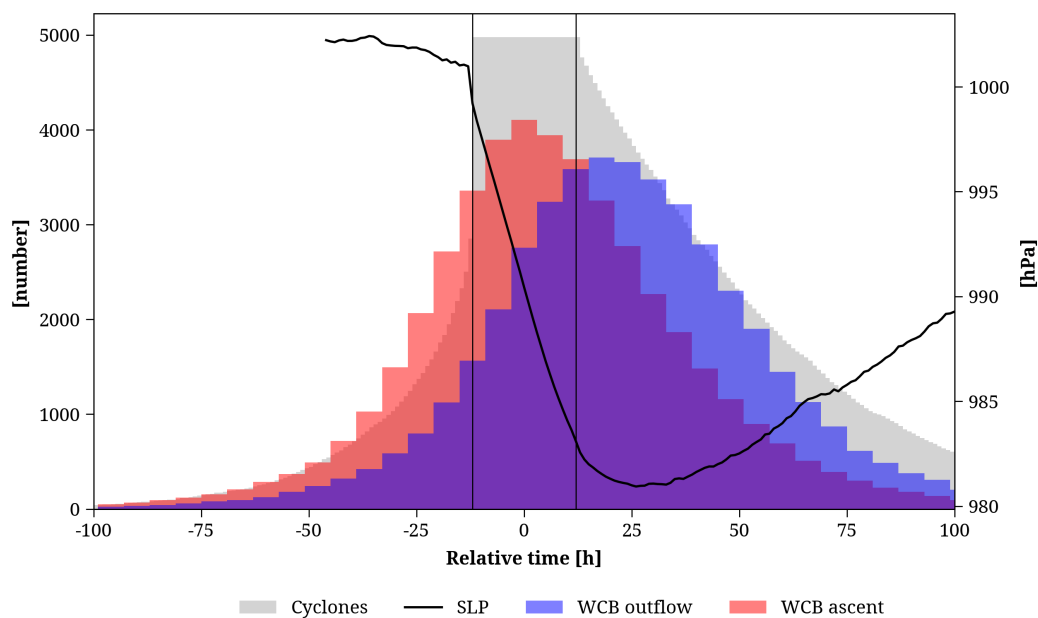
Figure 13. Number of selected cyclones (grey) and their associated WCB ascent (red) and outflow masks (blue) at different time instances during the cyclone life cycle, centered around the time of strongest cyclone deepening (see text for details). The average pressure of this subset of cyclones (hPa, black line) is shown for time instances with at least 500 cyclones.

615 described by Wernli (1997) and Rossa et al. (2000), were also captured by our method, as well as the increase in the intensity of the cyclonic branch as qualitatively described by Wernli (1997). Furthermore, the WCB outflow was found to align with a ULPVA that intensified significantly along the cyclone life cycle.

4   Climatology for North Atlantic cyclones in winter

The method to quantify WCB characteristics and impacts was applied in the previous sections to selected case studies and
620 showed an interesting evolution of these metrics along the cyclone life cycle. As a specific aspect, we found distinct differences in the cyclone-relative location and magnitude of the respective ULPVA associated with the outflow of the cyclonic and anticyclonic branches of the WCB, and generally an increase in the intensity of the cyclonic branch during and after cyclone intensification. However, the three cases, all intense North Atlantic cyclones with explosive deepening, are not climatologically representative. Therefore, in the following, in order to put the results from the case studies into perspective, we quantify the
625 characteristics and impacts of all WCBs associated with a representative set of winter (December–February, DJF) cyclones in the North Atlantic to systematically study the evolution of these metrics and their variability along the cyclone life cycle (Sect. 4.1). The analysis also specifically considers differences between the cyclonic and anticyclonic branches of WCBs (Sect. 4.2). To this aim, we first selected a subset of cyclones in DJF from the ERA5 period 1980–2022 with a typical pressure evolution.

Specifically, we only consider cyclones with a maximum $\Delta \mathrm{SLP}_B > 0$, i.e. the cyclones have to exist for at least 24 h and expe-
630   rience a decrease in cental SLP during this period (see Sect. 2.4 for details concerning $\Delta \mathrm{SLP}_B$). About 8'700 cyclones fulfill
these criteria in the North Atlantic (cyclone track starts between 105°W–15°E and 20°N–80°N) in DJF between 1980–2022.
In the second step, we only consider cyclones that are linked to a WCB ascent mask at one point in their life cycle. This
criterion is fulfilled for 57% of all cyclones in the North Atlantic with a positive $\Delta \mathrm{SLP}_B$ (approx. 5000). Eckhardt et al. (2004)
investigated cyclones in the entire northern hemisphere and found 60% of all cyclones associated with a WCB. However, Eck-
635   hardt et al. (2004) applied different selection criteria for cyclones and WCBs, such as a cyclone deepening of at least 10 hPa.
Intriguingly, if we only consider cyclones in the northern hemisphere with a deepening rate of at least 0.4 Bergeron, which
corresponds to 10 hPa in 24 h at 60°N, we also find that 59.1% of these cyclones are accompanied by a WCB, consistent with
Eckhardt et al. (2004).

We then centered each cyclone track around the time of strongest 24-h intensification, with the center of the 24-h time window
640   defined as the relative time $t_{rel} = 0\,\mathrm{h}$. Figure 13 shows how often cyclones (grey bars) are present as a function of t_{rel}. The cy-
clone selection criteria mentioned above lead to a constant number of approx. 5'000 cyclones during the 24-h window between
$t_{rel} = -12\,\mathrm{h}$ to $+12\,\mathrm{h}$. The distribution is skewed towards later times in the cyclone life cycle, indicating that the strongest
intensification occurs more often in the early stages of the cyclone life cycle. The averaged evolution of the central SLP of
these cyclones (black line, Fig. 13) shows a value of about 1000 hPa before intensification and a drop to about 983 hPa during
645   the 24 h of maximum intensification. Most WCB ascent masks (red bars, Fig. 13) associated with this subset of cyclones are
present between $t_{rel} = -3\,\mathrm{h}$ to $+3\,\mathrm{h}$, thus during maximum cyclone intensification. In contrast, the largest number of WCB
outflow masks exist between $t_{rel} = 15\,\mathrm{h}$ to $21\,\mathrm{h}$. These variations in the number of WCB masks present during the cyclone life
cycle must be considered in the subsequent analysis.

The following results are based on WCB masks that contain at least 10 trajectories to ensure a sufficiently large WCB mask
650   area. Based on this set of cyclones and their WCBs, we will investigate how the region of frequent WCB ascent, the WCB
characteristic and impact metrics, and the cyclonic and anticyclonic branches of the WCB evolve during the cyclone life cycle.

4.1   Evolution of WCBs during the cyclone life cycle

Figure 14 illustrates the regions where WCBs of North Atlantic cyclones frequently ascend at different relative times of the
655   selected cyclones. As each WCB ascends in the vicinity of a cyclone, which generally moves from west to east, the region of
WCB ascent depends on t_{rel}. Prior to maximum cyclone intensification (blue contour, Fig. 14), WCBs ascend most often in
an elongated band from 95 to 40°W and south of 50°N, partially over southeastern North America. During the main cyclone
intensification phase, at $t_{rel} = 0\,\mathrm{h}$ (red contour, Fig. 14), the region of the WCB ascent shifts northeastward and is located
almost entirely over the open ocean. A day after the cyclone's main intensification phase, at $t_{rel} = 24\,\mathrm{h}$ (yellow contour,
660   Fig. 14), WCBs ascend most frequently in the northeastern North Atlantic, north of 30°N. The changes in the atmospheric
conditions associated with the shift in the region of frequent WCB ascent have to be considered when investigating the WCB
characteristics and impacts relative to the cyclone's life cycle.
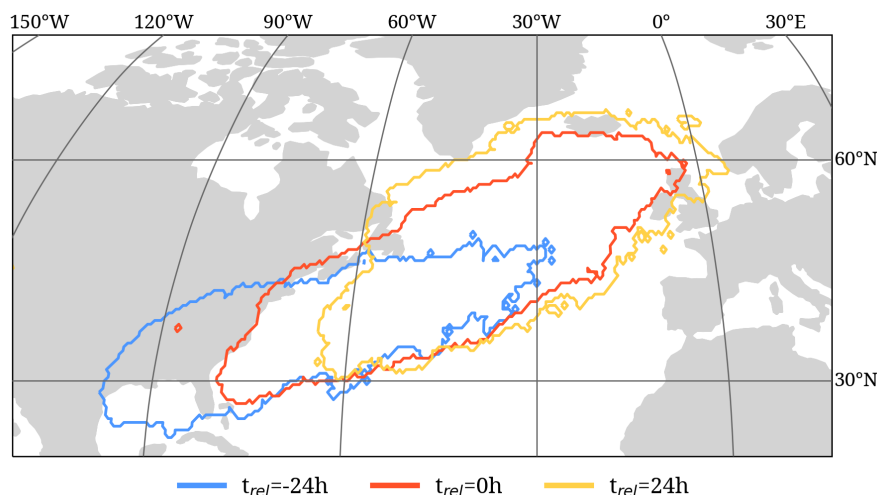
Figure 14. Regions of frequent WCB ascent before ($t_{rel} = -24$ h, blue), during ($t_{rel} = 0$ h, red) and after ($t_{rel} = +24$ h, yellow) the strongest cyclone intensification of the selected North Atlantic cyclones in DJF between 1980–2022. Due to the different number of WCB ascent masks present at each time step (Fig. 13), we show the 95th percentile contour of the respective WCB ascent mask frequency, namely $0.26, 0.68, 0.37\%$ at $t_{rel} = -24, 0, +24$ h, respectively.

Figure 15 presents the climatological evolution of the characteristics and impacts of the WCBs associated with the selected cyclones. At each time instance, we average the respective metrics over all WCB masks that are present. As shown in Fig. 13,

665 this number of WCB masks varies during the cyclone life cycle. The intensity of WCBs (black line, Fig. 15a) peaks at $t_{rel} = 5$ h with on average 325 trajectories per ascent mask. Slightly more trajectories ascend towards the end of the intensification period (318 trajectories) compared to the beginning (258 trajectories). The intensity of the WCB outflow (grey line, Fig. 15a) peaks at $t_{rel} = 23$ h. The delay in the averaged WCB intensity between ascent and outflow mask is very similar to the time difference in the peak number of WCB ascent and outflow masks, shown in Fig. 13 and can be explained by the time needed for

670 WCB trajectories to ascend from the middle to the upper troposphere. WCBs ascend most rapidly ($83.8\,\mathrm{hPa}\,(3\,\mathrm{h})^{-1}$, Fig. 15b) during the intensification phase ($t_{rel} = 4$ h). In contrast to the WCB intensity, the WCB ascent rate decreases distinctively after $t_{rel} = 0$ h. The percentage of cyclonically ascending trajectories (Fig. 15c) increases from about 7 to 18% between $t_{rel} = -20$ h to $+20$ h, while the share of anticyclonically ascending trajectories decreases from about 37 to 30% between $t_{rel} = -48$ h to $+48$ h. Notably, once the central pressure of the cyclones reaches its minimum, the percentage of cyclonically ascending

675 trajectories does not increase further. Overall, during cyclone intensification ($t_{rel} = -3$ h to $+3$ h), a distinct cyclonic branch with a relative intensity $> 20\%$ occurs in about 32% of the WCB ascent masks present at this time (red bars in Fig. 13). The altitude of the WCB outflow (Fig. 15d) decreases with time, as indicated by the increasing pressure of the trajectories that define the outflow mask. The propagation of the WCB during the cyclone life cycle (Fig. 14) to higher latitudes and, thus, to regions with a climatological lower tropopause explains the decreasing WCB outflow altitude.
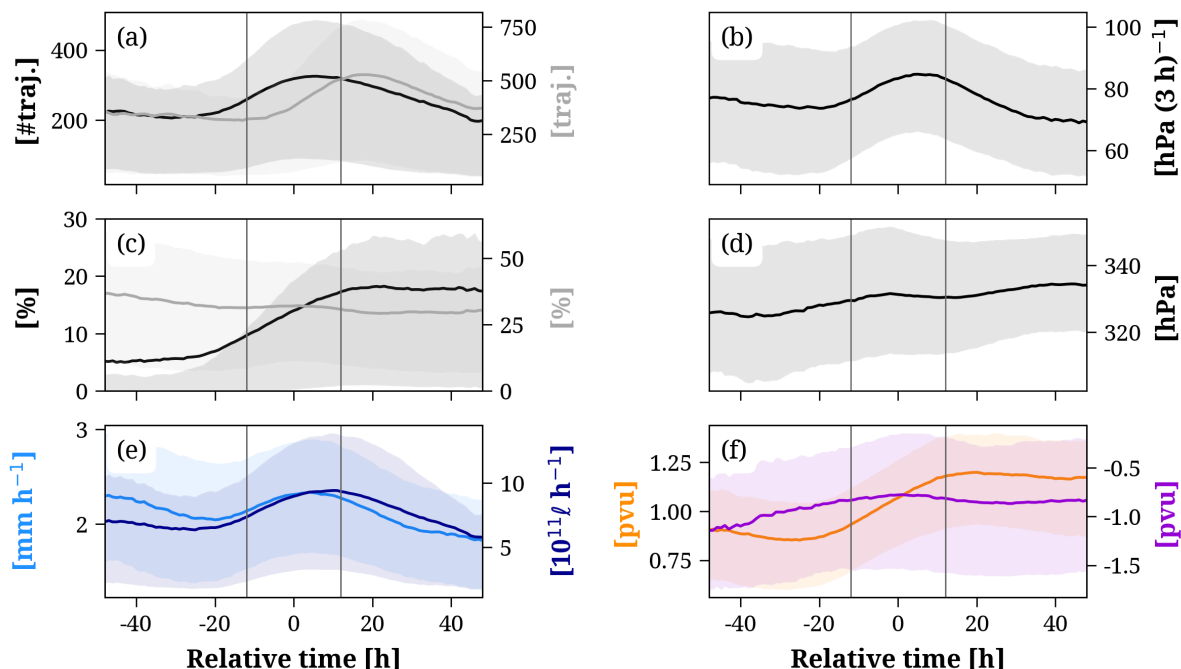
Figure 15. Mean (solid) and 50% confidence interval (shading) of the WCB metrics centered around the time of maximum cyclone intensification ($t_{rel} = 0$ h) for WCBs ascending in the North Atlantic in DJF between 1980–2022. (a) Intensity of the WCB ascent (number of trajectories, black) and outflow (number of trajectories, grey), (b) WCB ascent rate (hPa $(3\,\text{h})^{-1}$), (c) percentage of cyclonically (black) and anticyclonically ascending trajectories (%, grey), (d) outflow altitude (hPa), (e) PQ90 (mm h^{-1}, light blue) and PVOL ($10^{12}\,\ell\,\text{h}^{-1}$, dark blue), and (f) LLPV (pvu, orange) and ULPVA (pvu, purple). Vertical lines denote the 24-h period of strongest cyclone intensification.

680   Consistent with the presented case studies (Sect. 3), WCB-related impacts also depend on the cyclone-relative time in the climatology. The most intense PQ90 associated with WCBs (2.3 mm h^{-1}, light blue, Fig. 15e) is produced at $t_{rel} = 4$ h. The largest PVOL (dark blue, Fig. 15e) occurs 6 h later at $t_{rel} = 10$ h, linked to the also delayed peak in WCB intensity. The PQ90 is also enhanced during the early stages of the cyclone life cycle, very likely related to intense convective precipitation, which peaks at $t_{rel} = -48$ h (1.1 mm h^{-1}, not shown) when the WCB ascent occurs at lower latitudes (Fig. 14). However, it is

685   important to keep in mind that these heavy precipitation rates at early times occur only rarely, as shown by the relatively low number of WCB ascent masks at $t_{rel} < -30$ h (Fig. 13).

Latent heating linked to precipitation formation affects the LLPV in the region of the WCB ascent. In fact, Fig. 15f (orange line) shows that LLPV gradually increases from 0.85 pvu at $t_{rel} = -25$ h to 1.20 pvu at $t_{rel} = 20$ h. After $t_{rel} = 12$ h, when the pressure in the cyclone center reaches its minimum, the LLPV also remains fairly constant. Additionally to the PV production

690   by latent heat release, LLPV also increases with t_{rel} because of the northward displacement (Fig. 14) and the associated increase in the Coriolis parameter. The WCB impact on the PV in the upper troposphere (purple line, Fig. 15f) also varies with time but less distinctively. The ULPVA is most intense (negative) in the early stages of the cyclone life cycle. This

finding, however, is statistically less robust, as only a small number of WCB outflow masks is present before the cyclone's

intensification (blue bars, Fig. 13). As the intensity of the WCB outflow increases during cyclone intensification (Fig. 15b), the

695   ULPVA becomes slightly more intense and decreases from -0.78 pvu at $t_{rel} = 0$ h to -0.87 pvu at $t_{rel} = 28$ h. In contrast to

the median of the upper-level PV anomaly in the region of the WCB outflow (ULPVA), the respective 90th percentile is more

negative overall and decreases more distinctively after cyclone intensification (not shown).

So far, we investigated how the WCB metrics depend on the cyclone-relative time and considered all North Atlantic cyclones

characterized by a positive ΔSLP_B that are associated with a WCB. When focusing only on cyclones with stronger deepening

700   rates, WCB characteristics and impacts become more intense, whereas their overall temporal evolution remains similar (see Fig.

S3 in supplementary material). For instance, WCBs associated with cyclones with $\Delta SLP_B >1$ (so-called "bomb cyclones",

Sanders and Gyakum, 1980) are also most intense during the maximum intensification period (Fig. S3a) but reach average

WCB intensities of about 484 trajectories. In addition, these WCBs ascend more rapidly (max. $93\,\mathrm{hPa\,(3\,h)^{-1}}$, Fig. S3b) and

have a more intense cyclonically curved branch (max. 21%, Fig. S3c). The altitude of the outflow of WCBs (Fig. S3d) is not

705   affected by the intensity of the associated cyclone. In terms of WCB-related impacts, they are associated with larger PQ90

(max. $2.7\,\mathrm{mm\,h^{-1}}$, Fig. S3e), larger PVOL ($13.4 \cdot 10^{12}\,\ell\,\mathrm{h^{-1}}$, Fig. S3e), more intense LLPV after the cyclone intensification

phase (max. 1.24 pvu, Fig. S3f) and more negative ULPVA (-1.13 pvu, Fig. S3f) throughout the entire cyclone life cycle.

Thus, more strongly intensifying cyclones are associated with more intense WCB characteristics and impacts.

These findings about the evolution of WCB metrics along cyclone life cycles in the North Atlantic are also qualitatively valid

710   for WCBs in other regions. The climatological evolution of the characteristics and impacts of WCBs ascending in the respective

winter season in the North Pacific (105°E–110°W, 20°N–80°N), South Atlantic (65°W–10°E, 15°S–60°S) and South Pacific

(150°E–70°W, 15°S–60°S) is shown in Fig. S4 in the supplementary material. North Pacific WCBs show higher values of

WCB intensity, ascent rate, and PQ90 compared to WCBs ascending in other regions (Fig. S4a,b,e). The outflow of WCBs

ascending in the Southern Hemisphere reaches higher altitudes than in the Northern Hemisphere (Fig. S4d). The increase in

715   the share of cyclonically ascending trajectories (Fig. S4c) is similar in all regions but reaches the largest values in the North

Atlantic. While the LLPV increases most strongly in the North Pacific (Fig. S4e), the ULPVA becomes most intense in the

South Atlantic (Fig. S4f).

4.2   Differences in the outflow of the cyclonic, anticyclonic, and non-curved WCB branches

The case studies presented in Sect. 3 showed that the branches of the WCB differed in their outflow location relative to the

720   cyclone as well as the ULPVA values within the respective outflow masks. In the following, we generalize these findings by

comparing the outflow of the cyclonic, anticyclonic, and non-curved branches of all WCBs ascending in the North Atlantic

in DJF between 1980–2022. Each WCB outflow mask is now subdivided depending on the curvature of the underlying WCB

trajectories, as described in Sect. 2.4 and illustrated in the case studies (Fig. 5, 8, 11g-i). As in the previous sections, each

WCB outflow mask must contain at least 10 trajectories to ensure a sufficient mask area to calculate statistical values. For

725   this analysis, we only consider WCB outflow masks in the 6-h time window around $t_{rel} = 24$ h, thus during the peak in WCB

outflow intensity.
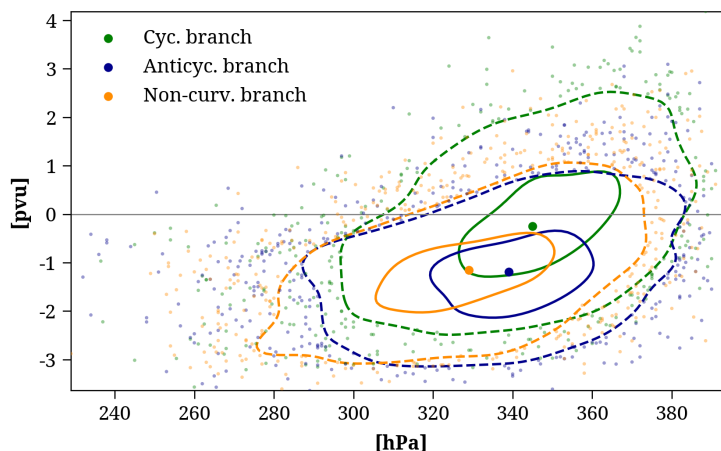
Figure 16. ULPVA (pvu) and pressure level (hPa) of the cyclonic (green), anticyclonic (blue), and non-curved (orange) WCB outflow at $t_{rel} = 24\,h$. A Gaussian kernel density function of the ULPVA and pressure level was used to define the solid (dashed) contours containing 30% (85%) of all data points. Large dots inside the solid contours show the median values, while the small dots show values outside the 85% density contour.

The resulting set of WCB outflow masks can be separated into 1828, 2397, and 2772 masks formed by the cyclonic, anticyclonic, and non-curved branches of the WCB, respectively. These numbers are smaller than the number of WCB outflow masks between $t_{rel} = 21\,h$ h to $27\,h$ shown in Fig. 13 (blue bars), due to the threshold of 10 trajectories for single WCB branches instead of the entire WCB outflow. The difference in the number of outflow masks associated with the different WCB branches indicates that WCBs are more likely to feature an anticyclonic branch than a cyclonic branch at this moment in the cyclone life cycle.

Figure 16a shows a scatter plot of the outflow pressure level and the ULPVA of the cyclonic, anticyclonic, and non-curved WCB branches. Independent of the curvature, both variables correlate positively (Spearman correlation coefficient $\rho = 0.45$). Due to the increasing climatological PV with altitude, higher WCB outflow altitudes lead to stronger negative PV anomalies. The intense diabatic heating occurring during the WCB ascent strengthens the cross-isentropic transport to the upper troposphere and leads to diabatic PV destruction above the level of maximum heating and, thus, to the formation of negative PV anomalies. Some WCB outflow regions are associated with positive ULPVA if they are located at relatively low altitudes (recall that ULPVA is calculated in a fixed vertical layer).

Consistent with the presented case studies, the amplitude of the ULPVA varies across the outflow of the cyclonic, anticyclonic, and non-curved WCB branches. The cyclonic WCB branch ascends to the lowest pressure levels ($345\,hPa$, median) and is associated with the weakest ULPVA ($-0.25\,pvu$, median), while the anticyclonic branch reaches higher altitudes ($339\,hPa$, median) and is linked to the strongest ULPVA ($-1.19\,pvu$, median). Although the anticyclonic and non-curved WCB branches are associated with a very similar ULPVA, the outflow of the non-curved WCB branch is located $10\,hPa$ above the anticyclonic

745 branch. As illustrated in Fig. 3, the anticyclonic branch bends eastward when reaching the upper-level flow at the northern edge of the ridge. In contrast, the non-curved WCB branch mainly ascends ahead of the upstream trough and towards the center of the ridge, where the tropopause height is enhanced, thereby potentially allowing for a higher WCB outflow altitude.

In summary, the systematic investigation of WCB branches is consistent with findings from the case studies. The anticyclonic and non-curved WCB branches are characterized by greater intensity, higher outflow altitude, and also a more intense ULPVA

750 than the cyclonic branch.

5   Discussion and conclusions

This section aims to answer the research questions posed in Section 1. First, we compare the case studies (Section 3) and then summarize the main findings from the climatological analysis (Section 4). Additionally, we discuss the results in the context of previous studies on cyclone life cycles and WCBs, address potential caveats and limitations of the developed method and

755 finish with the main conclusions and a brief outlook.

5.1   Comparison of case studies

Although all three case study cyclones showed a strong deepening, the temporal evolution of the associated WCBs differed in some key elements. First, the onset of the WCB can either coincide with the genesis of the cyclone or it may precede the

760 cyclone. In the IOP4 storm of 1989, the WCB was first detected in the ascent layer (500–800 hPa) about 12 h after cyclogenesis. In contrast, the WCB ascent of the 2009 case first occurs ahead of an upper-level trough about 18 h before cyclogenesis. The temporal shift in the third case was even larger, with the WCB ascent first occurring approximately 60 h before cyclogenesis, caused by the ascent ahead of an elongated upper-level PV streamer. The complex synoptic situation in the 2009 and 1992 cases required a manual attribution of trajectories to the respective cyclones. Thus, such early onsets of the WCB relative to the

765 cyclone life cycle are not included in the objective method to attribute WCB masks to cyclones presented in the climatology. In all three cases, the WCB started to weaken when the cyclone reached its maximum intensity. However, the three cases differed in their maximum WCB intensity. During the 1992 case, about 1000 trajectories formed the WCB ascent mask, twice as many as during the first and second cases. A reason for this could be the widespread upper-level forcing in the third case, which favors the ascent of air over a large region. Another explanation could be different amounts of moisture transported by the

770 WCB. However, this characteristic of the WCB was not considered in this study.

Another qualitative key difference between the cases concerns the formation of a cyclonic branch. While the share of cyclonically ascending trajectories increased to 63% and 49% in the second and third cases, respectively, it reached only 10% in the first case. Regarding WCB-related impacts, in the first two cases, PQ90 was most intense around the cyclone's intensification period. In contrast, in the third case, the most intense PQ90 occurred when the WCB ascended at low latitudes early in the

775 cyclone's life cycle. In all three cases, the period of enhanced PQ90 went along with enhanced ascent rates. The PVOL peaked around the cyclone's intensification period for all three cases. Its temporal evolution is linked to the corresponding evolution

of the WCB intensity and precipitation rates. During the 2009 case, PVOL peaked in a phase of weaker WCB intensity. This could be related to the relatively high PQ90 at this stage in the cyclone life cycle.

All three cases showed a clear increase in low-level PV in the area of WCB ascent. In the 2009 and 1992 cases, LLPV in-
780 creased gradually over three days from $0.5\,\mathrm{pvu}$ to $1.5\,\mathrm{pvu}$. In the 1989 case, LLPV increased rapidly from $0.5\,\mathrm{pvu}$ to $1.75\,\mathrm{pvu}$ within just $24\,\mathrm{h}$ during the cyclone intensification period. This period was also associated with the cyclone's exceptionally high deepening and precipitation rates, coinciding with the WCB ascent near the cyclone center leading to diabatically produced low-level PV. When the region of the WCB ascent migrated away from the cyclone center, the PQ90 and, consistently, the LLPV decreased. In contrast, the 2009 and 1992 WCBs were associated with less rapidly intensifying cyclones and weaker
785 precipitation rates, ascending largely at a greater distance to the cyclone center.

At upper levels, the temporal evolution of the PV anomaly in the region of the WCB outflow differed between the cases. In the 1989 and 1992 cases, the ULPVA was strongest 12–$24\,\mathrm{h}$ after the main cyclone intensification period and after the peak in WCB intensity. The intensification of the ULPVA was strongest for the 1989 WCB, potentially linked to the intense precipitation rates, thus, strong latent heat release, which potentially leads to a higher WCB outflow altitude. As a result, the WCB
790 outflow was characterized by a ULPVA of around $-2\,\mathrm{pvu}$. The ULPVA was similarly negative for the 1992 case, which had an extremely intense WCB. The strong cyclonic branch resulted in a westward extension of the WCB outflow region, where ULPVA was much weaker.

The selected case studies exhibited a maximum ΔSLP_B greater than 1 Bergeron. However, the cyclones included in the climatological analysis of WCB metrics in Section 3 were generally weaker, with an average maximum ΔSLP_B value of
795 0.5 Bergeron. Except for the weak cyclonic branch during the 2009 WCB case, all WCB metrics were more intense for the case studies than the corresponding climatological maximum values. For instance, climatological WCB ascent masks include approximately 300 trajectories during the cyclone intensification, whereas all three case studies experienced maximum WCB intensities exceeding 500 trajectories. The quantitative agreement between the case studies and the climatology improves if the latter only contains cyclones with a maximum ΔSLP_B greater than 1 Bergeron (see Fig. S3 in supplementary material).

800

5.2 Main findings from climatological analysis

The climatological analysis shows a clear pattern of how the WCB metrics vary along the life cycle of the corresponding cyclones, in qualitative agreement with the detailed results shown in the case studies. These main patterns are briefly summarized and put in context with related earlier findings in the literature:

805   – The intensity of the WCB ascent phase, i.e., of the period when WCB trajectories ascend through the layer from 800 to $500\,\mathrm{hPa}$, peaks during the period of maximum cyclone intensification. The intensity of the WCB outflow, i.e., when the trajectories rise within the layer above $400\,\mathrm{hPa}$, peaks about $18\,\mathrm{h}$ later. The results about the WCB ascent appear consistent with the fact that also the quasi-geostrophic upper-level forcing for ascent at $700\,\mathrm{hPa}$, evaluated in the vicinity of the cyclone center, peaks during maximum cyclone intensification (Besson et al., 2021). A reasonable interpretation

810   might be that the upper-level forcing for ascent at the same time contributes to vortex stretching in the cyclone center, and hence, cyclone intensification, as well as to the ascent of air from the warm sector, and hence WCB intensity. This interpretation is in line with results from a recent MSc thesis (Müürsepp, 2022), which quantified the relationship between quasi-geostrophic forcing for ascent and the WCB intensity.

815 – WCB ascent rates are not only related to large-scale quasi-geostrophic forcing for the WCB ascent. Also, thermodynamic stability, potentially leading to embedded convection, can lead to locally amplified WCB ascent rates (e.g., Oertel et al., 2019). Although the overall understanding of embedded convection in WCBs is still incomplete, it is likely that this phenomenon occurs preferentially at lower latitudes and, therefore, comparatively early in the life cycle of cyclones. This could explain the slightly enhanced WCB ascent rates and rates of convective precipitation around $t_{rel} = -40\,\mathrm{h}$. However, overall, the composite time evolution of WCB ascent and precipitation rates agrees remarkably well with the
820   evolution of WCB ascent intensity.

  – The share of cyclonically ascending WCB trajectories increases during the cyclone life cycle. This finding is consistent with previous qualitative descriptions of the flow evolution in extratropical cyclones. As described by Palmén (1951), the depth of the cyclonic circulation in a cyclone increases during its intensification, eventually affecting a large part of the troposphere. The increasing depth of the cyclonic circulation leads to an increasing number of WCB trajectories
825   that ascends cyclonically, as summarized by Schultz and Vaughan (2011). However, not every WCB features a distinct cyclonic branch, and it remains unclear which ambient flow conditions are favorable for the formation of a cyclonic branch. In all three case studies, pronounced cyclonic upper-level wave breaking (of type LC2 according to Thorncroft et al. (1993)) went along with the formation of a prominent cyclonic branch, but it is left for future investigations whether this result can be regarded as climatologically representative.

830 – Considering the two metrics for precipitation, PQ90 is largest during the cyclone's intensification phase and, thus, before it reaches the deepest SLP. This result is consistent with previous studies that found cyclone-related precipitation, which is mainly linked to the WCB ascent (Browning, 1990, Pfahl et al., 2014), to peak prior to the maximum cyclone intensity (Bengtsson et al., 2009, Michaelis et al., 2017, Hawcroft et al., 2017, Booth et al., 2018). The integrated metric PVOL peaks about 10 h after the peak in PQ90 at the end of the maximum cyclone intensification phase.

835 – The climatology of LLPV along the cyclone life cycle revealed an increase during cyclone intensification, which appears intuitive as the increased WCB-related LLPV can be an important factor for cyclone intensification (Binder et al., 2016). Several studies discussed in detail the factors that contribute to strong diabatic PV production in WCBs (Joos and Wernli, 2012; Madonna et al., 2014b; Binder et al., 2016), and emphasized, for instance, the role of the Coriolis parameter f. The poleward displacement of the cyclone and WCB goes along with an increase in f and hence absolute vorticity, which,
840   for a given vertical gradient of latent heating, increases the diabatic PV production.

  – At upper levels, the WCB outflow is associated with a negative PV anomaly throughout the cyclone life cycle. This finding is consistent with the results of Madonna et al. (2014b), who compared the PV of WCB trajectories 48 h after

their start with the climatological mean PV at the same position. They found PV anomalies between 0 to -3 pvu in the North Atlantic. The weaker ULPVA in this study (between about -0.3 and -1.5 pvu) is related to the different approach, as we calculate ULPVA in a fixed vertical layer (200–375 hPa, see Section 2.2), which captures not only the levels of the WCB outflow, as in Madonna et al., 2014b, but also ambient levels. The ULPVA becomes slightly stronger when the WCB outflow intensity peaks. The importance of the negative PV anomaly in the WCB outflow for the downstream large-scale flow evolution is determined not only by the intensity but also by the area of the PV anomaly. Thus, the largest impact of the WCB on the downstream large-scale flow evolution likely occurs about a day after the strongest cyclone intensification, when ULPVA is most negative, and the WCB outflow intensity is largest.

- As a particularly novel analysis, we systematically investigated the outflow level and ULPVA of the cyclonic, anticyclonic, and non-curved WCB branches, respectively. Consistent with the results from the case studies, the anticyclonic and non-curved branches ascend to higher altitudes and are associated with more intense ULPVA than the cyclonic branch. Already Wernli (1997), Martínez-Alvarado et al. (2014) and Blanchard et al. (2021) found for the anticyclonic branch of the WCB lower PV values on higher isentropes, typically corresponding to more negative PV anomalies, compared to the cyclonic branch. Our study shows that this important difference between WCB branches is a relatively robust feature, even if the case-to-case variability, as shown in Fig. 15, is high.

5.3 Limitations

This study demonstrates the potential of the developed method to systematically quantify various important characteristics and impacts of WCBs. However, due to the large variability of cyclones and WCBs, performing a purely objective analysis remains challenging. For instance, attributing WCBs to cyclones can be difficult, particularly in complex synoptic situations. We decided to attribute each WCB trajectory cluster to the cyclone with which it overlaps the most strongly while ascending between 800 and 600 hPa, similar to a study by Binder et al. (2023). However, this method may lead to an incorrect attribution in some cases, such as when a WCB is initially linked to a small cyclone, but its main ascent occurs later in a second cyclone. We tested various attribution algorithms, and the presented method agreed best with results from manual attribution. We are therefore confident that the benefit of this method offsets the occasional incorrect attributions. Other limitations of our approach are related to the choices of our metrics. Clearly, there would be alternative options to define parameters like ULPVA and WCB curvature, and there might also be other characteristics and metrics that would be worth investigating (e.g., more detailed cloud microphysical aspects like the vertical extent of the WCB cloud or microphysical rates of precipitation formation or freezing).

5.4 Main conclusions and outlook

This study introduces an objective approach to quantitatively assess a set of so-called characteristics and impacts of WCBs and applies this approach to three detailed case studies and a climatology of North Atlantic cyclones and their WCBs in 42 winters of ERA5 data.

The calculation of the WCB characteristics and impacts is based on a new WCB climatology. As in previous studies, a La-

875 grangian perspective is used, and WCBs are identified as coherent bundles of trajectories that ascend at least 600 hPa within a two-day time window, whereas the selection criteria for WCB trajectories are slightly adapted compared to Madonna et al. (2014b) (see section 2.2 for details). Based on this Lagrangian WCB climatology, at every 6-h time step, two-dimensional Eulerian masks of WCB inflow, ascent, and outflow are determined from the trajectories. We present a novel climatology of the frequency of occurrence of these different WCB masks, an approach that takes a diverse trajectory ascent behavior into

880 account. Then, we calculate different metrics within these masks. The considered metrics are intensity (number of trajectories within the mask), ascent rate (mean pressure change in 3 h), ascent curvature, precipitation rate (90th percentile of precipitation within the mask), the total precipitation volume in the mask, PV at low levels in the region of WCB ascent, and eventually PV anomalies in the region of WCB outflow. With this set of WCB metrics, which can be applied in other studies about WCBs identified in reanalyses or output from numerical weather prediction and climate simulations, this study offers an objective and

885 valuable framework to better quantify various relevant aspects of WCBs.

The main novelties of this study are (i) the systematic approach that yields interesting insight for detailed case studies but can also be used for climatological investigations, (ii) the cyclone life cycle perspective, which considers the evolution of the WCB metrics along the development of the associated cyclone, and (iii) the specific consideration of the differences between cyclonic and anticyclonic WCB branches. With regard to point (ii), it was shown with a large set of about 5'000 North Atlantic

890 winter cyclones, that the period of maximum cyclone intensification coincides with the maximum intensity of the WCB ascent, with peaks in surface precipitation and 3-h ascent rates, and with an increase in low-level PV and of the intensity of the cyclonically-curved branch of the WCB. This temporal synchronization of cyclone intensification and several key aspects of WCBs points to the dynamical linkages between dynamical forcing for ascent, cloud formation, precipitation, latent heating, diabatic PV production at low levels, and cyclone intensity.

895 As a brief outlook, we mention two extensions of this WCB characterization study. First, it could be rewarding to investigate statistical relationships between WCB characteristics and impacts, e.g., the correlations between WCB intensity and PVOL or between ascent rate and precipitation rates. And second, the multi-dimensional metrics could be determined for WCBs identified in climate simulations to identify potential effects of climate change on WCB characteristics (e.g., will their maximum ascent rate increase?), WCB impacts and their correlations. Joos et al. (2023) and Binder et al. (2023) were the first to identify

900 WCBs based on air parcel trajectories with wind fields from climate simulations. Comparing WCBs in the present-day climate and a future climate according to the RCP8.5 scenario, they found that WCBs will become more intense, moister, and associated with more intense precipitation. The approaches developed in this study might be ideal for obtaining further insight into the important questions of how WCBs and their multi-faceted characteristics and hydrological and dynamical impacts may be modified by anthropogenic warming.

905 *Code and data availability.* ERA5 reanalyses are available from the ECMWF website (https:// www.ecmwf.int/en/forecasts/datasets/reanalysis-datasets/era5).

Author contributions. KH performed the analyses and wrote the first version of this paper. All co-authors contributed to the design of the study, the interpretation of the results, and the writing.

Competing interests. The authors declare that they have no conflict of interest. HW is an executive editor of WCD.

910 *Acknowledgements.* This research has been supported by the Swiss National Science Foundation (SNSF) (grant no. 185049). The authors are grateful for valuable discussions with John Methven and Ambrogio Volonté (University of Reading).

References

Bengtsson, L., Hodges, K. I., and Keenlyside, N.: Will extratropical storms intensify in a warmer climate?, J. Clim., 22, 2276–2301, https://doi.org/10.1175/2008JCLI2678.1, 2009.

Besson, P., Fischer, L. J., Schemm, S., and Sprenger, M.: A global analysis of the dry-dynamic forcing during cyclone growth and propagation, Weather Clim. Dynam., 2, 991–1009, https://doi.org/10.5194/wcd-2-991-2021, 2021.

Binder, H., Boettcher, M., Joos, H., and Wernli, H.: The role of warm conveyor belts for the intensification of extratropical cyclones in Northern Hemisphere winter, J. Atmos. Sci., 73, 3997–4020, https://doi.org/10.1175/JAS-D-15-0302.1, 2016.

Binder, H., Boettcher, M., Joos, H., Sprenger, M., and Wernli, H.: Vertical cloud structure of warm conveyor belts–a comparison and evaluation of ERA5 reanalysis, CloudSat and CALIPSO data, Weather Clim. Dynam., 1, 577–595, https://doi.org/10.5194/wcd-1-577-2020, 2020.

Binder, H., Joos, H., Sprenger, M., and Wernli, H.: Warm conveyor belts in present-day and future climate simulations–Part 2: Role of potential vorticity production for cyclone intensification, Weather Clim. Dynam., 4, 19–37, https://doi.org/10.5194/wcd-4-19-2023, 2023.

Binder, H. V.: Warm conveyor belts: cloud structure and role for cyclone dynamics and extreme events, PhD Thesis, ETH Zurich, Zurich, 2017.

Blanchard, N., Pantillon, F., Chaboureau, J.-P., and Delanoë, J.: Organization of convective ascents in a warm conveyor belt, Weather Clim. Dynam., 1, 617–634, https://doi.org/10.5194/wcd-1-617-2020, 2020.

Blanchard, N., Pantillon, F., Chaboureau, J.-P., and Delanoë, J.: Mid-level convection in a warm conveyor belt accelerates the jet stream, Weather Clim. Dynam., 2, 37–53, https://doi.org/10.5194/wcd-2-37-2021, 2021.

Booth, J. F., Thompson, L., Patoux, J., and Kelly, K. A.: Sensitivity of Midlatitude Storm Intensification to Perturbations in the Sea Surface Temperature near the Gulf Stream, Mon. Weather Rev., 140, 1241–1256, https://doi.org/10.1175/MWR-D-11-00195.1, 2012.

Booth, J. F., Naud, C. M., and Jeyaratnam, J.: Extratropical cyclone precipitation life cycles: A satellite-based analysis, Geophys. Res. Lett., 45, 8647–8654, https://doi.org//10.1029/2018GL078977, 2018.

Browning, K.: Organization of clouds and precipitation in extratropical cyclones, in: Extratropical cyclones, pp. 129–153, Springer, https://doi.org/10.1007/978-1-944970-33-8_8, 1990.

Browning, K. and Roberts, N.: Structure of a frontal cyclone, Q. J. Roy. Meteor. Soc., 120, 1535–1557, https://doi.org/10.1002/qj.49712052006, 1994.

Browning, K., Hardman, M., Harrold, T., and Pardoe, C.: The structure of rainbands within a mid-latitude depression, Q. J. Roy. Meteor. Soc., 99, 215–231, https://doi.org/10.1002/qj.49709942002, 1973.

Carlson, T. N.: Airflow through midlatitude cyclones and the comma cloud pattern, Mon. Weather Rev., 108, 1498–1509, https://doi.org/10.1175/1520-0493(1980)108<1498:ATMCAT>2.0.CO;2, 1980.

Catto, J.: Extratropical cyclone classification and its use in climate studies, Rev. Geophys., 54, 486–520, https://doi.org/10.1002/2016rg000519, 2016.

Catto, J. L., Madonna, E., Joos, H., Rudeva, I., and Simmonds, I.: Global relationship between fronts and warm conveyor belts and the impact on extreme precipitation, J. Clim., 28, 8411–8429, https://doi.org/10.1175/JCLI-D-15-0171.1, 2015.

Chagnon, J. M., Gray, S. L., and Methven, J.: Diabatic processes modifying potential vorticity in a North Atlantic cyclone: Diabatic Modification of Potential Vorticity, Q. J. Roy. Meteor. Soc., 139, 1270–1282, https://doi.org/10.1002/qj.2037, 2013.

Eckhardt, S., Stohl, A., Wernli, H., James, P., Forster, C., and Spichtinger, N.: A 15-year climatology of warm conveyor belts, J. Clim., 17, 218–237, https://doi.org/10.1175/1520-0442(2004)017<0218:AYCOWC>2.0.CO;2, 2004.

950 Flaounas, E., Kotroni, V., Lagouvardos, K., Gray, S. L., Rysman, J.-F., and Claud, C.: Heavy rainfall in Mediterranean cyclones. Part I: contribution of deep convection and warm conveyor belt, Clim. Dyn., 50, 2935–2949, https://doi.org/10.1007/s00382-017-3783-x, 2018.

Grams, C. M., Wernli, H., Böttcher, M., Čampa, J., Corsmeier, U., Jones, S. C., Keller, J. H., Lenz, C.-J., and Wiegand, L.: The key role of diabatic processes in modifying the upper-tropospheric wave guide: a North Atlantic case-study, Q. J. Roy. Meteor. Soc., 137, 2174–2193, https://doi.org/10.1002/qj.891, 2011.

955 Grams, C. M., Magnusson, L., and Madonna, E.: An atmospheric dynamics perspective on the amplification and propagation of forecast error in numerical weather prediction models: A case study, Q. J. Roy. Meteor. Soc., 144, 2577–2591, https://doi.org/10.1002/qj.3353, 2018.

Harrold, T.: Mechanisms influencing the distribution of precipitation within baroclinic disturbances, Q. J. Roy. Meteor. Soc., 99, 232–251, https://doi.org/10.1002/qj.49709942003, 1973.

Hawcroft, M., Dacre, H., Forbes, R., Hodges, K., Shaffrey, L., and Stein, T.: Using satellite and reanalysis data to evaluate the representation
960 of latent heating in extratropical cyclones in a climate model, Clim. Dyn., 48, 2255–2278, https://doi.org/10.1007/s00382-016-3204-6, 2017.

Hersbach, H., Bell, B., Berrisford, P., Hirahara, S., Horányi, A., Muñoz-Sabater, J., Nicolas, J., Peubey, C., Radu, R., Schepers, D., and others: The ERA5 global reanalysis, Q. J. Roy. Meteor. Soc., 146, 1999–2049, https://doi.org/10.1002/qj.3803, 2020.

Joos, H. and Forbes, R. M.: Impact of different IFS microphysics on a warm conveyor belt and the downstream flow evolution, Q. J. Roy.
965 Meteor. Soc., 142, 2727–2739, https://doi.org/10.1002/qj.2863, 2016.

Joos, H. and Wernli, H.: Influence of microphysical processes on the potential vorticity development in a warm conveyor belt: a case-study with the limited-area model COSMO, Q. J. Roy. Meteor. Soc., 138, 407–418, https://doi.org/10.1002/qj.934, 2012.

Joos, H., Sprenger, M., Binder, H., Beyerle, U., and Wernli, H.: Warm conveyor belts in present-day and future climate simulations–Part 1: Climatology and impacts, Weather Clim. Dynam., 4, 133–155, https://doi.org/10.5194/wcd-4-133-2023, 2023.

970 Knippertz, P., Chagnon, J. M., Foster, A., Lathouwers, L., Marsham, J. H., Methven, J., and Parker, D. J.: Research flight observations of a prefrontal gravity wave near the southwestern UK, Weather, 65, 293–297, https://doi.org/10.1002/wea.632, 2010.

Madonna, E., Limbach, S., Aebi, C., Joos, H., Wernli, H., and Martius, O.: On the Co-Occurrence of Warm Conveyor Belt Outflows and PV Streamers*, J. Atmos. Sci., 71, 3668–3673, https://doi.org/10.1175/JAS-D-14-0119.1, 2014a.

Madonna, E., Wernli, H., Joos, H., and Martius, O.: Warm conveyor belts in the ERA-Interim dataset (1979–2010). Part I: Climatology and
975 potential vorticity evolution, J. Clim., 27, 3–26, https://doi.org/10.1175/JCLI-D-12-00720.1, 2014b.

Martínez-Alvarado, O., Joos, H., Chagnon, J., Boettcher, M., Gray, S., Plant, R., Methven, J., and Wernli, H.: The dichotomous structure of the warm conveyor belt, Q. J. Roy. Meteor. Soc., 140, 1809–1824, https://doi.org/10.1002/qj.2276, 2014.

Methven, J.: Potential vorticity in warm conveyor belt outflow, Q. J. Roy. Meteor. Soc., 141, 1065–1071, https://doi.org/10.1002/qj.2393, 2015.

980 Michaelis, A. C., Willison, J., Lackmann, G. M., and Robinson, W. A.: Changes in winter North Atlantic extratropical cyclones in high-resolution regional pseudo–global warming simulations, J. Clim., 30, 6905–6925, https://doi.org/10.1175/JCLI-D-16-0697.1, 2017.

Müürsepp, T.: Warm Conveyor Belts in the Extratropics: What Determines Their Intensity?, Master's thesis, ETH Zurich, Zurich, https://doi.org/10.3929/ethz-b-000600318, 2022.

Namias, J.: The use of isentropic analysis in short term forecasting, J. Aeronaut. Sci., 6, 295–298, https://doi.org/10.2514/8.860, 1939.

985   Neiman, P. J. and Shapiro, M.: The life cycle of an extratropical marine cyclone. Part I: Frontal-cyclone evolution and thermodynamic air-sea interaction, Mon. Weather Rev., 121, 2153–2176, https://doi.org/10.1175/1520-0493(1993)121<2153:TLCOAE>2.0.CO;2, 1993.

Neiman, P. J., Shapiro, M., and Fedor, L.: The life cycle of an extratropical marine cyclone. Part II: Mesoscale structure and diagnostics, Mon. Weather Rev., 121, 2177–2199, https://doi.org/10.1175/1520-0493(1993)121<2177:TLCOAE>2.0.CO;2, 1993.

Neu, U., Akperov, M. G., Bellenbaum, N., Benestad, R., Blender, R., Caballero, R., Cocozza, A., Dacre, H. F., Feng, Y., Fraedrich, K.,
990   Grieger, J., Gulev, S., Hanley, J., Hewson, T., Inatsu, M., Keay, K., Kew, S. F., Kindem, I., Leckebusch, G. C., Liberato, M. L. R., Lionello, P., Mokhov, I. I., Pinto, J. G., Raible, C. C., Reale, M., Rudeva, I., Schuster, M., Simmonds, I., Sinclair, M., Sprenger, M., Tilinina, N. D., Trigo, I. F., Ulbrich, S., Ulbrich, U., Wang, X. L., and Wernli, H.: IMILAST: A Community Effort to Intercompare Extratropical Cyclone Detection and Tracking Algorithms, B. Am. Meteorol. Soc., 94, 529–547, https://doi.org/10.1175/BAMS-D-11-00154.1, 2013.

Oertel, A., Boettcher, M., Joos, H., Sprenger, M., Konow, H., Hagen, M., and Wernli, H.: Convective activity in an extratropical cyclone and
995   its warm conveyor belt–a case-study combining observations and a convection-permitting model simulation, Q. J. Roy. Meteor. Soc., 145, 1406–1426, https://doi.org/10.1002/qj.3500, 2019.

Oertel, A., Boettcher, M., Joos, H., Sprenger, M., and Wernli, H.: Potential vorticity structure of embedded convection in a warm conveyor belt and its relevance for large-scale dynamics, Weather Clim. Dynam., 1, 127–153, https://doi.org/10.5194/wcd-1-127-2020, 2020.

Palmén, E.: The aerology of extratropical disturbances, Compendium of Meteorology: Prepared under the Direction of the Committee on the
1000   Compendium of Meteorology, pp. 599–620, https://doi.org/10.1007/978-1-940033-70-9_49, 1951.

Pfahl, S., Madonna, E., Boettcher, M., Joos, H., and Wernli, H.: Warm conveyor belts in the ERA-Interim dataset (1979–2010). Part II: Moisture origin and relevance for precipitation, J. Clim., 27, 27–40, https://doi.org/10.1175/JCLI-D-13-00223.1, 2014.

Pfahl, S., Schwierz, C., Croci-Maspoli, M., Grams, C. M., and Wernli, H.: Importance of latent heat release in ascending air streams for atmospheric blocking, Nat. Geosci., 8, 610–614, https://doi.org/10.1038/ngeo2487, 2015.

1005   Rasp, S., Selz, T., and Craig, G. C.: Convective and slantwise trajectory ascent in convection-permitting simulations of midlatitude cyclones, Mon. Weather Rev., 144, https://doi.org/10.1175/MWR-D-16-0112.1, 2016.

Reed, R. J. and Danielsen, E. F.: Fronts in the vicinity of the tropopause, Archiv für Meteorologie, Geophysik und Bioklimatologie, Ser. A, Meteorologie und Geophysik, 11, 1–17, https://doi.org/10.1007/BF02247637, 1958.

Rodwell, M., Forbes, R., and Wernli, H.: Why warm conveyor belts matter in NWP, ECMWF newsletter, 154, 21–28,
1010   https://doi.org/10.21957/mr20vg, 2018.

Rossa, A. M., Wernli, H., and Davies, H. C.: Growth and Decay of an Extra-Tropical Cyclone's PV-Tower, Meteorology and Atmospheric Physics, 73, 139–156, https://doi.org/10.1007/s007030050070, 2000.

Röthlisberger, M., Martius, O., and Wernli, H.: Northern Hemisphere Rossby wave initiation events on the extratropical jet—A climatological analysis, J. Clim., 31, 743–760, https://doi.org/10.1175/JCLI-D-17-0346.1, 2018.

1015   Sanders, F. and Gyakum, J. R.: Synoptic-dynamic climatology of the "bomb", Mon. Weather Rev., 108, 1589–1606, https://doi.org/10.1175/1520-0493(1980)108<1589:SDCOT>2.0.CO;2, 1980.

Schemm, S. and Wernli, H.: The Linkage between the Warm and the Cold Conveyor Belts in an Idealized Extratropical Cyclone*, J. Atmos. Sci., 71, 1443–1459, https://doi.org/10.1175/JAS-D-13-0177.1, 2014.

Schultz, D. M. and Vaughan, G.: Occluded fronts and the occlusion process: A fresh look at conventional wisdom, B. Am. Meteorol. Soc.,
1020   92, 443–466, https://doi.org/10.1175/2010BAMS3057.1, 2011.

Schäfler, A., Craig, G., Wernli, H., Arbogast, P., Doyle, J. D., McTaggart-Cowan, R., Methven, J., Rivière, G., Ament, F., Boettcher, M., and others: The North Atlantic waveguide and downstream impact experiment, B. Am. Meteorol. Soc., 99, 1607–1637, https://doi.org/10.1175/BAMS-D-17-0003.1, 2018.

Sprenger, M. and Wernli, H.: The LAGRANTO Lagrangian analysis tool–version 2.0, Geo. Sci. Model Dev., 8, 2569–2586, https://doi.org/10.5194/gmd-8-2569-2015, 2015.

Sprenger, M., Fragkoulidis, G., Binder, H., Croci-Maspoli, M., Graf, P., Grams, C. M., Knippertz, P., Madonna, E., Schemm, S., Škerlak, B., and others: Global climatologies of Eulerian and Lagrangian flow features based on ERA-Interim, B. Am. Meteorol. Soc., 98, 1739–1748, https://doi.org/10.1175/BAMS-D-15-00299.1, 2017.

Steinfeld, D. and Pfahl, S.: The role of latent heating in atmospheric blocking dynamics: a global climatology, Clim. Dyn., 53, 6159–6180, https://doi.org/10.1007/s00382-019-04919-6, 2019.

Stoelinga, M. T.: A potential vorticity-based study of the role of diabatic heating and friction in a numerically simulated baroclinic cyclone, Mon. Weather Rev., 124, 849–874, https://doi.org/10.1175/1520-0493(1996)124<0849:APVBSO>2.0.CO;2, 1996.

Stohl, A.: A 1-year Lagrangian "climatology" of airstreams in the northern hemisphere troposphere and lowermost stratosphere, J. Geophys. Res. - Atmos, 106, 7263–7279, https://doi.org/10.1029/2000JD900570, 2001.

Thorncroft, C., Hoskins, B., and McIntyre, M.: Two paradigms of baroclinic-wave life-cycle behaviour, Q. J. Roy. Meteor. Soc., 119, 17–55, https://doi.org/10.1002/qj.49711950903, 1993.

Wernli, H.: A Lagrangian-based analysis of extratropical cyclones. II: A detailed case-study, Q. J. Roy. Meteor. Soc., 123, 1677–1706, https://doi.org/10.1002/qj.49712354211, 1997.

Wernli, H. and Davies, H. C.: A Lagrangian-based analysis of extratropical cyclones. I: The method and some applications, Q. J. Roy. Meteor. Soc., 123, 467–489, https://doi.org/10.1002/qj.49712353811, 1997.

Wernli, H. and Schwierz, C.: Surface cyclones in the ERA-40 dataset (1958–2001). Part I: Novel identification method and global climatology, J. Atmos. Sci., 63, 2486–2507, https://doi.org/10.1175/JAS3766.1, 2006.